An analytical and numerical investigation into conductive-radiative energy transfers in evacuated honeycombs. Application to the optimisation and design of ultra-high temperature thermal insulation.

An analytical and numerical investigation into conductive-radiative energy transfers in evacuated honeycombs. Application to the optimisation and design of ultra-high temperature thermal insulation.

Thibaut Desguers*, Adam Robinson

Institute for Energy Systems, School of Engineering, University of Edinburgh, Max Born Crescent, Edinburgh EH9 3BF, Scotland, United Kingdom

Abstract

Ultra-high temperature thermal and latent energy storage technologies offer a potential solution to the decarbonisation of the energy sector. However, uneconomical thermal energy losses are a barrier to their development and where significant, their minimisation requires knowledge about the different modes of thermal transport and their interaction in a given structure. In this paper, evacuated rectangular honeycomb structures are investigated as candidates for efficient ultra-high temperature thermal insulation.

First, a theory is laid out along with its numerical implementation for the modelling of coupled non-linear conduction and radiation in three-dimensional cuboid multi-media structures with rarefied gaseous and opaque or semi-transparent solid media. The model is then applied to the study, optimisation and design of efficient ultra-high temperature thermal insulation based on rectangular honeycomb structures.

A dimensionless number N_{rc} is defined and an analytical thermal analysis of rectangular honeycombs is developed which correlates N_{rc} to the optimal geometry and equivalent thermal conductivity of a honeycomb insulator. A numerical optimisation procedure is then presented and the correlations are validated, and thus constitute simple practical design tools for honeycomb insulators. Finally, it is shown that with an appropriate choice of geometry and materials, thin-walled honeycombs have the capacity to outperform existing high-temperature thermal insulation technologies with thermal conductivities lower than 0.01 W/m/K at 1600K. In particular, a wall thickness of 50μm on a titanium alloy honeycomb would suffice to outperform ceramic fibre insulation over its entire range of operating temperatures.

Keywords: Heat Transfer, Honeycomb, High temperature, Thermal insulation, Combined conduction and radiation, Rarefied gas

1. Introduction

Today, high capacity energy storage remains one of the major obstacles to a full-scale development and implementation of renewable energy technologies, without which hundred-percent decarbonised electricity grid, power and heating integrated networks will not be achievable. Unfortunately, it would not be economically viable to rely on current grid-connected storage technologies to provide enough capacity to compensate for the inherent intermittency of renewables, since most suffer from low energy densities, low efficiencies, long-term degradation or inconvenient deployment location requirements [1].

Ultra-high temperatures (UHT) (∼1800K) would ensure

*Corresponding author

Email address: thibaut.desguers@ed.ac.uk (Thibaut Desguers)

greater energy densities and allow heat engine extraction cycles to operate at higher efficiencies, consequently improving the overall round-trip energy efficiency - see, for example, an Ultra-High Temperature Thermal Storage (UHTS) system presented by Robinson [2, 3] or Datas' UHT latent heat thermal store [4]. However with higher operating temperatures come additional energy losses which prove increasingly difficult to prevent as radiative transfers become predominant, and efficient ultra-high temperature technologies for thermal insulation are needed.

Vacuum insulated panels can achieve thermal conductivities as low as 0.004 W/m/K at room temperature [5, 6]. However, they suffer from high cost, thermal bridging and decreasing thermal properties through time [5], and they are only operable at low temperatures typically encountered in building applications. Commercially available insulating materials and technologies with a maximum service temperature higher than 1200K include fire bricks, vermiculite boards, silica-based microporous boards and ceramic fibre blankets. Of all these, ceramic fibre insulation has the highest operation temperature of up to 1673K, and the best thermal performance as they exhibit high-temperature ($\sim$ 1400K) equivalent thermal conductivities as low as 0.05W/m/K at about 13Pa [7]. This paper investigates evacuated honeycomb structures as potential candidates to both improve thermal performance at such temperatures and raise the maximum operating temperature to UHTS requirements with similar thermal performance.

The problem of radiative interchange within cavity or honeycomb structures has gathered much attention for many years. Early studies [8–12] focused on purely radiative transfers within an opaque enclosure. Later investigations accounted for conductive and convective transfers [13–15], however decoupled models were used whereby the total heat transfer is calculated as the sum of a purely radiative and purely conductive (or convective) heat transfer. This was later shown to greatly underpredict the global heat transfer [16] and the coupling, first introduced by Ref. [17], was later accounted for [16, 18]. The Radiative Transport Equation (RTE) was then needed for the modelling of opaque cavities with opaque obstacles and proved to give satisfactory results in the case of grey materials and a purely radiative heat transfer [19, 20]. The RTE was then applied to semi-transparent materials in conjunction with conductive transfers [21, 22], albeit in a single-medium structure and with a temperature-independent thermal conductivity. The non-linear conduction equation was solved for the case of an emitting, absorbing and scattering medium with non-grey properties [23] - however the solution was developed in one-dimension for a single-medium structure. Multi-media structures were later introduced [24], however wall conduction was ignored, and the gas thermal conductivity was considered constant. The case of a multiple building-block was studied by Antar [25] for opaque and grey walls, and solid conduction with constant thermal conductivity (together with convective transfer). More recently, a finite-element methodology was applied to the coupled conductive-radiative problem within cellular ceramics at high-temperature [26], however the study was limited to the case where solid media are opaque to thermal radiation.

To allow the study of honeycomb structures without these limitations, this paper presents a methodology which builds on the above-mentioned studies for the modelling of coupled conduction and radiation in three-dimensional complex rectangular multi-media structures with obstacles and internal boundaries of any kind. Media may be opaque or semi-transparent to thermal radiation with temperature-dependent and non-grey thermal and optical properties, so that radiative and conductive transfers may happen through participating (potentially rarefied) gaseous and solid media alike. Two or more media may be present, with multiple interfaces between them, and the Radiative Transport Equation (RTE) is fully solved in all participating media. To do so, the paper is organised as

follows. The geometries are introduced in section 2, while the theoretical model and its numerical implementation are detailed in section 3. The model is then applied to the study, optimisation and design of high-temperature thermal insulation based on evacuated honeycomb structures in section 4. The results are then summarised in section 5.

2. Geometries and materials

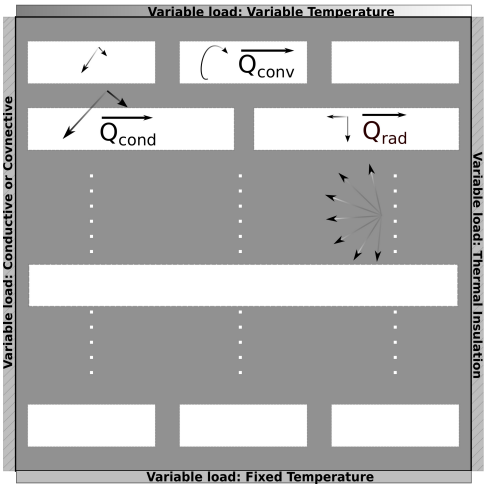

Figure 1: 2D-slice of example geometry with various boundary conditions and heat transfers

The present model is developed for any three-dimensional multi-media geometry consisting of a cuboid cavity filled with a network of cuboid solid elements and gas cells. All media may be opaque, semi-transparent or transparent to thermal radiation. Applications of these geometries may be seen in solar collectors, honeycombs, gas furnaces, combustion chambers and thermal insulation, the focus of this paper. In particular, this study focuses on a rectangular honeycomb with rectangular cells containing gas at low pressure as depicted in Fig.(1). The dimensions and spatial distributions of cells and wall thicknesses are parameters that can be varied for the study, design and optimisation of insulators based on this geometry (which can be extruded into the paper to form the third dimension. However the resulting profile may also be made to vary along that dimension).

Note that for a given cross-section, a square-angled cell has a smaller perimeter than a circular or hexagonal one, resulting in a larger conductive path (and therefore conductive resistance) from one side of the cell to the other. Also, smaller angles or curved edges allow surface elements on opposite sides of the cell to see each other (from a radiative perspective) more than they would with square angles. As a consequence, square-angled geometries are expected to be more efficient at inhibiting radiative and conductive transfers, which is why hexagonal and circular cells are not investigated here.

While a vacuum without solid structures would best insulate against conduction and convection, a compromise must be reached where radiative loss control is needed, as is the case for a UHTS system [2]. Honeycombs naturally emerge as potential candidates to achieve this as the evacuated cavities act as radiative shields without significantly enhancing conductive (and, in semi-transparent media, radiative) energy transfers if the walls are optimised. Such structures are studied as static insulators (i.e without a flow) and are filled with air at low pressure ($\sim$10Pa).

Although the present methodology is not restricted to particular materials or dimensions, all applications are carried out for conditions relevant to UHT operation. Typical operating hot and cold temperatures are of order 1600K and 288K, respectively. Two categories of solid materials with respect to thermal radiation are considered: semi-transparent and opaque. Ceramic alumina (Al_2O_3) is chosen as an example of the former (for reasons laid out in Ref. [2, 3]) while stainless steel of type 321 (thereafter ss321) will be used to illustrate the latter. The criteria for opacity and semi-transparency is discussed in Appendix A.

3. Theoretical model and numerical formulation

3.1. Governing equations

Thermal energy transfers may occur in the form of conduction in the gas and through solid walls, convection in the gas and at the boundaries, and radiation through the gas and solid and at the boundaries. In steady state, and in the absence of internal energy generation, the conservation of energy within a given medium leads to

$$\nabla \cdot [\mathbf{q_{cond}} + \mathbf{q_{conv}} + \mathbf{q_{rad}}] = 0 \tag{1}$$

where $\mathbf{q}$ denotes a heat flux for a particular mode of thermal transfer. Typical Grashof numbers for geometries presently considered are a few orders of magnitude lower than critical values reported in the literature for microchannels [27, 28] so that convection transfers can be ignored ($\mathbf{q_{conv}} = \mathbf{0}$), which allows Eq.(1) to be rewritten as

$$\nabla \cdot [-k(T) \times \nabla(T)] = S_t(T) \tag{2}$$

where T is the local temperature, k is the local thermal conductivity, spatial dependencies have been omitted for clarity, and $S_t = -\nabla \cdot \mathbf{q_{rad}}$ is the radiative source term coupling conductive and radiative transports. Lifting the conductive non-linearity of Eq. (2) by means of a Kirchhoff transform leads to

$$\Delta \tilde{T} = -S_t(T) \tag{3}$$

where $\tilde{T}$ is the transformed temperature. The Kirchhoff transform is used as it allows for an exact treatment of the conductive non-linearity, thereby eliminating the need for numerical approximations. The only remaining source of non-linearity now stems from the radiative source term which cannot be further simplified and must be resolved separately with the Radiative Transport Equation (RTE, see section 3.3). The RTE and energy conservation equation (Eq.(3)) are coupled and must therefore be solved simultaneously, and separately in the gas and solid as they have different local thermal and optical properties.

Once the transformed temperature field has been obtained, the local conductive heat flux is given by:

$$\mathbf{q_c} = -\nabla \tilde{T} \tag{4}$$

The temperature field may then be obtained by applying the corresponding inverse Kirchhoff transform to $\tilde{T}$.

3.2. Conductive transfer

3.2.1. Conductive properties of solids

Data for alumina can be found in Karditsas & Baptiste [29] for temperatures ranging from 298K to 1600K, while values for ss321 for temperatures from 1K to 1672K are reported in Ho & Chu [30].

3.2.2. Gaseous transport and rarefaction effects

A Sutherland-type formula is used for gaseous conductivity k at standard temperature and pressure conditions (STP):

$$k(T) = C_0 \frac{T^{3/2}}{T + T_0} \tag{5}$$

with C_0=0.00277 W/m/K$^{1.5}$ and T_0=280.6 K for air. However, this equation only holds within the framework of classical continuum fluid dynamics, *i.e* for a gas where inter-molecular collisions are the dominant mode of transport, which happens when the mean free path is significantly smaller than a typical dimension of the vessel containing the fluid. Where this is not the case however, rarefaction effects may occur [31–33], the degree of which is quantified by the Knudsen number $Kn = l/L$ (a widely accepted classification of flow regimes based on Kn is given in Ref.[34]), where L is a characteristic dimension of the system and l is the mean-free path which is known from the kinetic theory of gases [31]. Here, two factors may contribute to rarefaction effects; low pressures and small cell dimensions, which were set precisely to minimise gaseous transfers by conduction and convection, and typical Kn values belong to the transition-flow regime, meaning that rarefaction effects must be accounted for.

In rarefied conditions, the thermal conductivity of a gas becomes dependent on the pressure, for which the use of a Bossanquet-type formula has been validated by several authors [35, 36]:

$$k(T,P) = \frac{k_0(T)}{1+\alpha Kn(T,P)} \tag{6}$$

where k_0 is the thermal conductivity at STP (Eq.(5)) and $\alpha = 2$ [35, 36] is a non-dimensional rarefaction parameter. Note that the rarefied gas theory was developed in terms of the gas viscosity; however the same mechanisms govern viscous and thermal energy transport, which validates the use of this theory for gaseous thermal conductivities [31].

3.3. Radiative transfer

3.3.1. Governing equations

In semi-transparent media, the spectral radiative intensity I_ν obeys the following equation:

$$\begin{aligned}(\mathbf{s}\cdot\nabla)I_\nu(\mathbf{r},\mathbf{s}) = \kappa_\nu(T)I_{b_\nu}(T) - \beta_\nu(T)I_\nu(\mathbf{r},\mathbf{s}) \\ + \frac{\sigma_\nu(T)}{4\pi}\int_{4\pi} I_\nu(\mathbf{r},\mathbf{s_0})\Phi(\mathbf{s},\mathbf{s_0})d\Omega\end{aligned} \tag{7}$$

where the subscript ν indicates spectral quantities, $\mathbf{r}$ is the position vector, $\mathbf{s}$ is the direction of propagation, Ω is the solid angle it subtends, σ_ν is the spectral scattering coefficient, $\beta_\nu = \kappa_\nu + \sigma_\nu$ where κ_ν is the spectral coefficient of absorption, Φ is the scattering phase function, and I_{b_ν} is the blackbody's spectral radiative intensity. Note that the frequency rather than the wavelength is used here since it remains unchanged as radiation propagates from one medium to another. Also in Eq.(7), it was assumed that rays propagate along straight lines so that the direction of propagation $\mathbf{s}$ is independent of the spatial variable $\mathbf{r}$ within a medium (the reader is referred to Sarvari [37] for a detailed treatment of radiative propagation with variable refractive indices).

The spectral radiative source term per unit volume, related to the spectral radiative heat flux $\mathbf{q}_{\mathbf{r}_\nu}$, is iven by

$$S_{t_\nu}(\mathbf{r}) = -\nabla\cdot\mathbf{q}_{\mathbf{r}_\nu} = -\kappa_\nu(T)\cdot[4\pi I_{b_\nu}(T) - G_\nu(\mathbf{r})] \tag{8}$$

where G_ν is the spectral irradiation

$$G_\nu(\mathbf{r}) = \int_{4\pi} I_\nu(\mathbf{r},\mathbf{s})d\Omega \tag{9}$$

and $\mathbf{q}_{\mathbf{r}_\nu}$ is the spectral radiative heat flux

$$\mathbf{q}_{\mathbf{r}_\nu}(\mathbf{r}) = \int_{4\pi} I_\nu(\mathbf{r},\mathbf{s})\mathbf{s}d\Omega \tag{10}$$

Notice that in the case of opaque media, the radiative source term is identically zero. Surface radiative energy gains or losses at the interface with semi-transparent media are then obtained from thermal boundary conditions (see section 3.4). Finally, the total quantities are calculated by integrating Eqs.(8-10) over the whole spectral range (see below).

Because of the RTE dependency on many variables, assumptions must be made on directionality: rough surfaces in honeycomb structures will be modelled as diffuse emitters (if opaque) and reflectors, whereas smooth surfaces will be modelled as specular directional reflectors and directional emitters (if opaque). For details on the validity of the diffuse assumption, see for example [10, 38–40].

3.3.2. Optical properties

Radiative spectrum. The frequency range used in this study for bodies at temperatures between 293K and 1600K is [$3.33\cdot10^{12}$-$6\cdot10^{14}$]Hz, corresponding to wavelengths of [0.1-90]μm in vacuum.

Optical constants and reflectivities. The macroscopic complex optical index m, index of refraction n and extinction index k are given by [41]

$$\begin{aligned}m &= n + ik \\ \epsilon &= \epsilon' + i\epsilon'' = m^2\end{aligned} \tag{11}$$

where ϵ' and ϵ'' are the real and imaginary parts of ϵ, the microscopic complex dielectric function. The aforementioned absorption coefficient is then calculated as:

$$\kappa_\nu = \frac{4\pi\nu k}{c_o} \tag{12}$$

where c_0 is the speed of light in vacuum. The complex dielectric function is theoretically described by the four-parameter-semi-quantum (FPSQ) model [42]. This theory applies to any solid-state material, and therefore so does the numerical procedure presented in the next section. However optical properties have been sought for the aforementioned example materials alumina and SS321 and are given in Appendix A.

Besides, some gases may participate in radiative transfers. However, radiation - gas interactions happen through transitions of molecular energy levels and, as such, require a dense enough molecular medium to be significant; at standard atmospheric conditions and moderate temperatures, for typical cavity sizes considered here (a few millimetres at most), dry air is transparent to radiation. In rarefied conditions, at a pressure of 10 Pa, the air density is a hundred-thousandth of its value at standard conditions, further reducing interactions with radiation to levels even more negligible. Consequently, air is treated as a non-participating gas in this study.

For a beam travelling from medium 1 to medium 2, the specular directional-hemispherical reflectance for lossy media is given by the generalised Fresnel coefficients [43–46]:

$$\begin{aligned} R_s(\theta_i) &= \left| \frac{\mu_2 m_1 \cos\theta_i - \mu_1 m_2 \cos\theta_r}{\mu_2 m_1 \cos\theta_i + \mu_1 m_2 \cos\theta_r} \right|^2 \\ R_p(\theta_i) &= \left| \frac{\epsilon_1 m_2 \cos\theta_r - \epsilon_2 m_1 \cos\theta_i}{\epsilon_1 m_2 \cos\theta_r + \epsilon_2 m_1 \cos\theta_i} \right|^2 \\ R_{tot} &= 0.5 \cdot (R_s + R_p) \end{aligned} \tag{13}$$

where $\mu_{1,2}$ are the complex magnetic permeabilities of both media, θ_i and θ_r are the angles of incidence and refraction, subscripts p and s denote the two different states of polarisation, and the last equation holds for unpolarised radiation. The angle of refraction for subcritical angles of incidence follows Snell's law

$$n_1 \sin\theta_i = n_2 \sin\theta_r \tag{14}$$

with more conditions applying for supercritical angles [46]. In the following, all materials will be assumed to be non-magnetic, so that magnetic permeabilities disappear from the above equations. Besides, for opaque materials, the reflectivity will be calculated from the emissivity and Kirchhoff's law.

For incidences lower than ∼60°, the reflected radiation intensity is approximately isotropic [40]. It is then convenient to define a diffuse reflectance as

$$\begin{aligned} R_{d_\nu} &= \frac{\iint R_\nu(\theta) I_\nu \cos\theta d\Omega}{\iint I_\nu \cos\theta d\Omega} \\ &= \int_0^{\pi/2} R_\nu(\theta) \sin(2\theta) d\theta \end{aligned} \tag{15}$$

where the second equality holds for a diffuse radiation intensity.

Other properties. Based on published studies [47], polarisation effects are ignored and the last line of Eq.(13) will be used. Also, as published data for the scattering coefficient and phase function are insufficient, scattering effects have been ignored in all 2D and 3D calculations and applications presented from section 3.5.4 onward. However for the sake of generality, scattering terms will be included in the following theoretical and numerical developments.

3.3.3. Radiative boundary conditions

Boundary conditions for the radiative intensity at an interface between an opaque wall and semi-transparent medium is, on the wall (w):

$$I_\nu(\mathbf{s}) = \epsilon_w I_{b_\nu}(T_w) + \frac{1-\epsilon_w}{\pi} \int_{\mathbf{n}\cdot\mathbf{s}'<0} I_\nu(\mathbf{s}') \left|\mathbf{n}\cdot\mathbf{s}'\right| d\Omega' \tag{16}$$

for a diffusely reflective surface, and

$$I_\nu(\mathbf{s}) = \epsilon_w(\theta_i) I_{b_\nu}(T_w) + (1-\epsilon_w(\theta_i)) I_\nu(\mathbf{s_i}) \tag{17}$$

for a specularly reflecting surface.

The interface between two semi-transparent media 1 and 2 must be treated differently. Referring to Fig.(2), an energy balance for specular reflectors and transmitters leads to [41]

$$I_{\nu_2}(\mathbf{s_{2r}}) = \rho_{21}(\theta_{2i}) I_{\nu_2}(\mathbf{s_{2i}}) + \frac{(1-\rho_{12}(\theta_{1i}))n_2^2}{n_1^2} I_{\nu_1}(\mathbf{s_{1i}}) \tag{18}$$

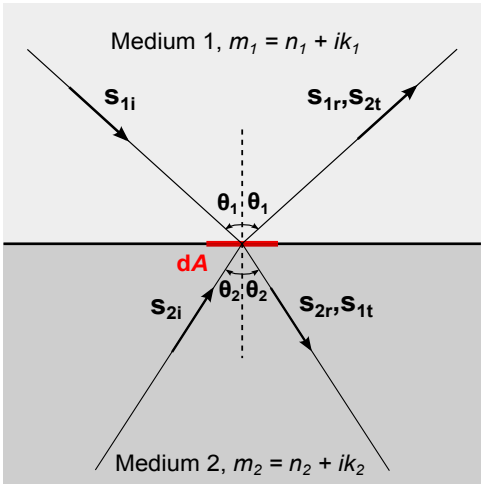

Figure 2: Radiative boundary conditions for two semi-transparent media

where ρ_{ij} is the reflectivity from medium i to medium j. A similar equation applies to medium 1.

In the presence of external irradiation, radiative transfers must be accounted for at the system's outer boundaries. For opaque ones, they are obtained using Eqs.(16,17) and surface properties to calculate the reflected intensity. For semi-transparent surfaces, Eq.(18) is used to calculate the outward radiative flux leaving the system which is then substituted in the interface thermal boundary condition (see below). In both cases, the external radiation field and optical index must be known.

3.4. Thermal boundary conditions

Equation.(3) can now be expressed as

$$\Delta\tilde{T} = \int_{\nu} \kappa_\nu(T) \cdot [4\pi I_{b_\nu}(T) - G_\nu(T)] d\nu \tag{19}$$

in semi-transparent materials, and

$$\Delta\tilde{T} = 0 \tag{20}$$

in opaque materials. To fully solve the problem, boundary conditions are needed at the system's outer boundaries, and may be of Dirichlet or Robin type. For the latter, a simple energy balance is performed with a combination of radiative and convective or conductive exchanges allowed with the outside.

Internal boundary conditions depend on the media on either side of it. When both are semi-transparent, the radiative flux is continuous across the surface and the thermal boundary condition reduces to the continuity of the conductive flux. If one medium is opaque, there exist no radiative flux within it, so that the sum of the conductive and radiative fluxes on the semi-transparent side of the interface equals the conductive flux on the opaque side. All fluxes at an interface are a function of the interface's temperature which is determined by these thermal boundary conditions.

3.5. Numerical formulation

3.5.1. Spatial discretisation: finite differences

A 3D Cartesian spatial discretisation is applied to the differential terms of Eqs.(4,19,20) using numerical approximations to first and second-order derivatives with respect to spatial variables. To accommodate boundary nodes and their neighbours, various combinations of central, forward and backward differences were used [48]. All numerical derivative estimates are 2^{nd} order accurate for both uniform and non-uniform grids, which were used for improved accuracy around interfaces and surfaces where sharper gradients are present.

3.5.2. RTE discretisation

The DOM method. The RTE has no known analytical solution for the present problem, and was therefore solved numerically with the Discrete Ordinates Method (thereafter DOM) using the step spatial differencing scheme [49] together with an EWO10 angular quadrature [50] which were found best suited for the present problem to mitigate ray effects and false scattering whilst satisfying the relevant closure criteria [51, 52]. For more details on how the DOM, the reader is referred to Refs.[21, 41, 52–56].

Diffuse transmission. Considered geometries involve obstacles and multi-media structures and, as such, internal

boundaries. While opaque interfaces are addressed using a discrete form of Eqs.(16,17), semi-transparent interfaces are handled as follows.

Irradiation incident upon an optically rough surface undergoes multiple reflections on surface irregularities. Besides, as it penetrates into the medium (over a small distance for an opaque interface), it is reflected off scattering centres multiple times, and part of it is scattered back towards the surface from which it came. These two reflection mechanisms cause the reflected radiation to emerge at a wide range of outgoing angles, which is known as diffuse reflection. But the same mechanisms also apply to rays incident from the other side and transmitted, which will encounter the same scattering centres as they propagate and emerge through the same rough surface, therefore also undergoing multiple reflections off scattering centres and surface irregularities, thus also emerging at a wide range of outgoing angles. Consequently transmission, along with reflection, may also be treated as diffuse in the present case.

The outgoing flux in medium 2 (see Fig.(2)), q_2^{out}, is given by

$$\begin{aligned} q_2^{out} &= \iint_{\mathbf{s_{2r}}\cdot\mathbf{n_2}>0} I_{\nu_2}(\mathbf{s_{2r}})\,|\mathbf{s_{2r}}\cdot\mathbf{n_2}|\,d\Omega_2 \\ &= \rho_{21}\iint_{\mathbf{s_{2r}}\cdot\mathbf{n_2}>0} I_{\nu_2}(\mathbf{s_{2i}})\,|\mathbf{s_{2r}}\cdot\mathbf{n_2}|\,d\Omega_2 \\ &+ \frac{(1-\rho_{12})n_2^2}{n_1^2}\iint_{\mathbf{s_{2r}}\cdot\mathbf{n_2}>0} I_{\nu_1}(\mathbf{s_{1i}})\,|\mathbf{s_{2r}}\cdot\mathbf{n_2}|\,d\Omega_2 \end{aligned} \tag{21}$$

where Eq.(18) has been used for the second equality. In this form, Eq.(21) cannot be discretised because of the second right hand side term which is the integral over all outgoing angles in medium 2 of a function depending on all incoming angles in medium 1; it must therefore be rewritten as an integral over all outgoing angles in medium 2. This is done using the definition of the spherical polar angle ($|\mathbf{s}\cdot\mathbf{n}| = \cos\theta$) and the associated solid angle, Snell's law (Eq.(14), along with the fact that incoming and outgoing angles in a given medium are equal) and its differentiated form ($n_1\cos\theta_1 d\theta_1 = n_2\cos\theta_2 d\theta_2$), which leads to

$$\begin{aligned} q_2^{out} &= \rho_{21}\iint_{\mathbf{s_{2i}}\cdot\mathbf{n_2}<0} I_{\nu_2}(\mathbf{s_{2i}})\cos\theta_2 d\Omega_2 \\ &+ (1-\rho_{12})\iint_{\mathbf{s_{1i}}\cdot\mathbf{n_1}<0} I_{\nu_1}(\mathbf{s_{1i}})\cos\theta_1 d\Omega_1 \end{aligned} \tag{22}$$

The integral of the first right-hand side term represents the incident flux in medium 2, q_2^{inc}, while that of the second term represents the incoming flux in medium 1, q_1^{inc}. Besides, under the assumption of diffuse transmission, the outgoing intensity in medium 2 is isotropic and related to q_2^{out} by $I_{\nu_2} = q_2^{out}/\pi$. Eq.(22) then takes its final compact form

$$I_{\nu_2}(\mathbf{s_{2r}}) = [\rho_{21}q_2^{inc} + (1-\rho_{12})q_1^{inc}]/\pi \ , \ \forall \mathbf{s_{2r}} \tag{23}$$

with a similar equation for $I_{\nu_1}(\mathbf{s_{1r}})$. Eq.(23) expresses the conservation of radiative energy at the interface, and takes this simple form only under the assumption of diffuse reflection and transmission. Eq.(23) is then discretised in the same way as Eqs.(16,17) and incorporated into the numerical scheme as an internal boundary conditions as described above.

It is important to note that the diffuse transmission assumption allows the same angular quadrature to be used throughout the entire geometry, eliminating the need to introduce new directions into the quadrature scheme after each incidence of specular transmission. This is because according to Eq.(23), the angles of incidence and transmission are not correlated.

3.5.3. General numerical scheme

Combining sections 3.5.1 and 3.5.2, Eq.(19) is formulated in matrix form

$$\mathbf{A}\cdot\tilde{\mathbf{t}} = \mathbf{b} \tag{24}$$

where $\tilde{\mathbf{t}}$ is a column vector of length n whose elements are the $\tilde{T}$ values at all n nodes, $\mathbf{A}$ is an n x n matrix containing all the numerical differential terms, and $\mathbf{b}$ is a column vector of size n containing the radiative terms

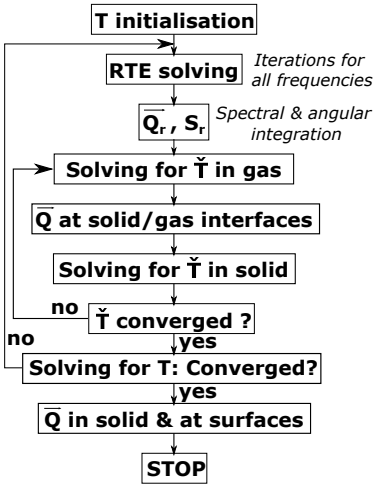

Figure 3: General numerical scheme

and energy transfers at interfaces and boundaries. The vector $\tilde{\mathbf{t}}$ is then obtained through matrix inversion, and an inverse Kirchhoff transform finally gives the temperature field.

Because $\mathbf{b}$ is a function of the temperature field T, an iterative scheme must be employed to solve Eqs.(19,20) once the radiative source term is known. The chosen general scheme for two media, summarised in Fig.(3), follows the one outlined in Ref.[57], and proceeds with two nested iteration loops as follows:

1. First, the grid is constructed, and the Kirchhoff operators are built. Then, the temperature field is initialised by solving the heat equation assuming a purely conductive heat transfer with constant thermal conductivities, which speeds up convergence.
2. The RTE is then solved for all frequencies following the procedure outlined in section 3.5.2. The total radiative fluxes and source terms are computed by angular and spectral integration, using numerical quadratures and Simpson's rule, respectively.
3. The heat equation is solved for $\tilde{T}$ according to section 3.5.1, with one nested loop of iterations necessary to establish thermal equilibrium between the two media for a given S_t. First, $\tilde{T}$ is obtained in medium 1, using the value of $\tilde{T}$ from the previous iteration as a Dirichlet boundary condition at interfaces with medium 2. Then, heat flux are calculated at the interfaces between the two media and then used as thermal boundary conditions to solve for $\tilde{T}$ in medium 2 as explained in section 3.4. This process is repeated until convergence of the $\tilde{T}$ field in both media. (In the presence of more than two media, each additional medium will require an extra nested loop of iterations to establish thermal equilibrium between it and the surrounding medium.)
4. When $\tilde{T}$ convergence is obtained, an inverse Kirchhoff transform gives the temperature field T. If convergence is achieved for T, the code moves on to step 5 below. Otherwise, it repeats steps 2 and 3 until T convergence is achieved.
5. The heat fluxes in the entire physical domain and heat flows at the system's boundaries are then calculated, and the process stops.

It is considered that the convergence of a given field F is achieved when the successive relative differences in F from one iteration (i) to the next (i+1) fall below a predefined threshold everywhere in the numerical domain:

$$\left| \frac{F_{i+1} - F_i}{F_{i+1}} \right| < \delta \tag{25}$$

where δ is usually set to 10^{-6}. Due to the non-linearities in the governing equations, convergence may require the use of under-relaxation [58].

The use of under-relaxation becomes increasingly necessary for convergence as the radiation to conduction ratio increases and gives rise to numerical instabilities, for example with higher temperatures or larger systems and, for semi-transparent materials, because of a larger conduction-radiation thermal coupling (see section 4.2.2). For instance, for the largest systems and highest temperatures considered in section 4, relaxation factors as low as 0.01 have been used, resulting in running times of up to half a day for a 526x488 2D grid. However, the relaxation

factor can be varied within a simulation and, in the present case, was first set to a low value to stabilise the numerical scheme, and then gradually increased to speed-up convergence. As a comparison, the smaller 3D systems tested in the next section below on a 144x58x12 3D grid take a few hours at most to complete.

3.5.4. 2D/3D convergence

The present methodology is adaptable to two-dimensional systems simply by omitting terms relevant to the z-direction in the equations, which allows to investigate three-dimensional effects. To do so, a rectangular honeycomb is chosen which contains 10 single-cell rows between the top and bottom surfaces which are maintained at 1200K and 288K respectively. Each cell is 2mm high and 10mm wide, and the wall thickness is 0.4mm everywhere. The honeycomb is studied in two and three dimensions with a range of forty depths ranging from 8mm to 5.1m, giving depth to height aspect ratios $\alpha = d/D_h$ between 0.33 and 209. The gas within the cells and around the honeycomb is air at a pressure of 10Pa. The honeycomb is perfectly insulated on its lateral external boundaries so that the thermal boundary conditions there are prescribed zero heat flux. Perfect radiative insulation is achieved by setting these boundaries to be perfect reflectors (*i.e* opaque with zero emissivity). For the three-dimensional system, the front and rear surfaces are transparent gaseous boundaries (the honeycomb is placed in a vacuum chamber at 288K), and perfect reflector solid boundaries.

Figure 4 shows the percentage difference (relative to the 3D value) in top surface heat flow for alumina and ss321. In both cases, the relative differences decrease with increasing depths. For alumina, there is a 53.2% difference for α=0.33. The differences then drop below the 10%, 5%, 1% and 0.5% marks for aspect ratios of 5.53, 11.7, 61.5 and 110.7, respectively. For ss321, the difference at α=0.33 is

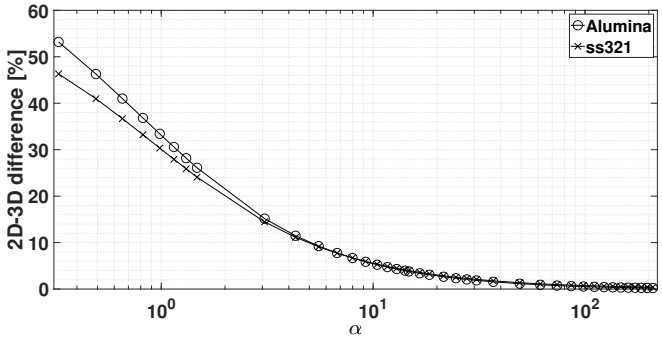

Figure 4: A comparison between the results of 2D and 3D top surface heat flows for several depth to height ratios for alumina and ss321. Notice the logarithmic scale on he x-axis.

46.3%, and drop below the same marks for aspect ratios of 5.53, 11.7, 73.8 and 159.8. The differences between the 2D and 3D geometries are caused by the radiative losses at the front and rear gaseous boundaries which cannot be accounted for in a 2D model; at these boundaries the open ducts, made fully transparent in the tests, freely exchange radiative energy with the vacuum chamber at 288K. The larger the depths, the less significant these exchanges are relative to the two-dimensional energy flow, which explains why the differences go down with increasing aspect ratios. These results prove the convergence of the three-dimensional solution towards the two-dimensional one for infinitely deep systems. Consequently, to reduce CPU requirements, the analysis in the remainder of this paper is carried out in two dimensions.

3.5.5. Grid independence

Grid independence of the numerical results is tested on a 2D alumina honeycomb of the same geometry and with the same boundary conditions as in the previous section. Five different spatial resolutions are tested: 0.2mm, 0.1mm, 0.05mm, 0.02mm and 0.01mm. Results are shown in Fig.(5). The successive differences are calculated by taking the difference between two successive Q estimates and then dividing it by the Q value obtained with the coarser grid. The energy flow curve (dashed line, square markers, left axis) is seen to flatten out as the number

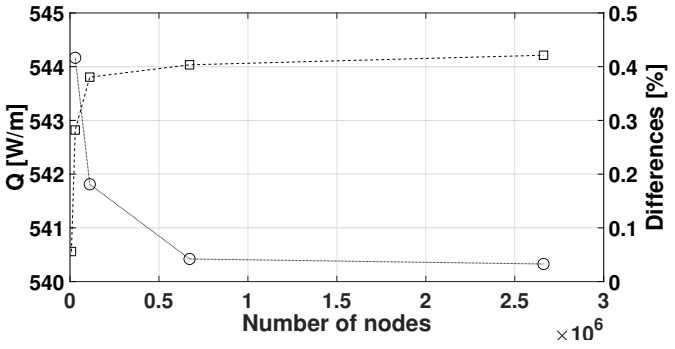

Figure 5: Grid independence test: energy transfer rate (square markers) and successive differences (round markers) for several spatial resolutions. Lines are visual guides only.

of nodes increases, which indicates convergence of the numerical solution. The successive differences curve (dotted line, round markers, right axis) also flattens out and shows values ranging from 0.42% for coarser grids to 0.03% difference for finer ones when the number of nodes is increased fourfold (last point on the curve). Antar [25] used a 0.5% change from a selected grid to the next as a criterion for grid selection; this is achieved for all grids in this example.

4. Optimisation: design tools and application to high temperature thermal insulation

4.1. Problem formulation

4.1.1. Objectives

We now apply the model to the design and optimisation of thermal insulators based on geometries represented in Fig.(1). The purpose of this study is to establish design criteria to meet specific performance requirements for a given application, to gain some insight into the physics of energy transport within such structures, and to study their thermal performance.

The study is conducted in two-dimensions (as per the results of section 3.5.4) and focuses on thermal optimisation only; no mechanical loads are considered. The honeycombs top and bottom surfaces are maintained at hot (T_h) and cold (T_c) temperatures (see section 4.1.2). The objective function to be minimised is the honeycomb's equivalent thermal conductivity, defined by

$$k_{eq} = Q/(T_h - T_c) \tag{26}$$

where Q is the total energy flow from the hot surface per unit depth.

4.1.2. Optimisable variables

Optimisable variables are selected by only retaining those geometrical and thermal parameters which have the greatest impact on the equivalent conductivity. The wall thickness is treated as a parameter of constant value t=0.4mm, both horizontally and vertically, and its impact on k_{eq} is explored in section 4.4. Besides, radiative and conductive transfers are both minimised with wide and narrow cells, so that only single-cell rows are considered (vertical columns become important only where structural strength is required). The number of cells, then equal to the number of rows, is an optimisable variable. As for the honeycomb size, in practice it is dictated by the dimensions of the gap the insulation has to fit in. But because scale effects are expected, four different scales are tested ({12.4, 24.4, 48.4, 72.4}mm), while larger ones are explored in section 4.4. Finally, to further simplify the study, cells of uniform height h are considered first, which leads to the following geometrical constraint between the number of cells N and their height h and width w:

$$\begin{aligned} D_h &= Nh + (N+1)t \\ w &= D_h - 2t \end{aligned} \tag{27}$$

Here N is chosen as the optimisable variable. For engineering purposes, the minimum cell size is set to the smallest commercially available for rectangular cell honeycombs which at the time of writing is around 2mm. However for theoretical purposes, smaller cells are investigated too.

The equivalent conductivity k_{eq} depends on the boundary conditions of which the number of combinations to account for all possible scenarios can be very large. However in practice the honeycomb width and depth for plane geometries are likely to be large, thereby minimising boundary

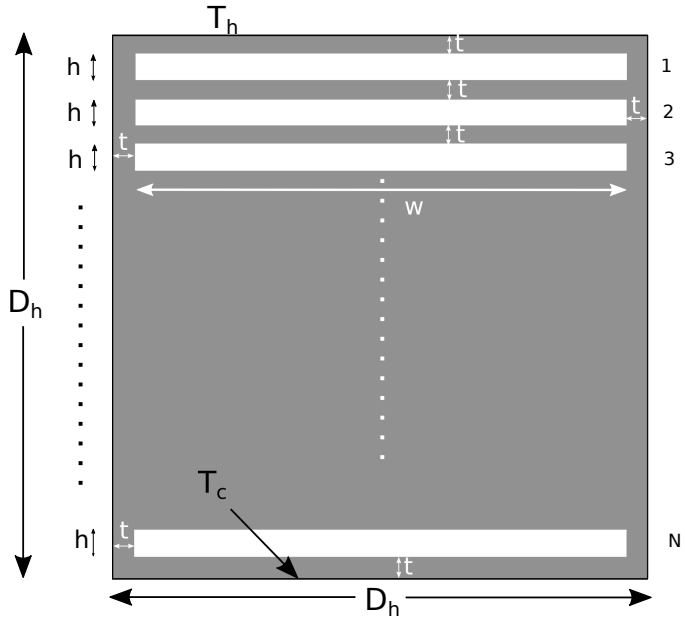

Figure 6: Optimisable honeycomb geometry for thermal optimisation. The boundary conditions are prescribed hot (resp. cold) temperature at the top (resp. bottom) surface, and zero heat flux on the sides

effects. Consequently, only one set of boundary conditions with fixed hot (T_h) and cold (T_c) temperatures at the top and bottom surfaces with zero heat flux on the lateral boundaries is chosen to best simulate realistic engineering applications. Four hot temperatures are considered ({400, 800, 1200, 1600}K for ss321 and {400, 650, 900, 1200}K for alumina), while the cold temperature is fixed to $T_c = 288$K. All structures are subject to a vacuum pressure of 10Pa. The resulting optimisable honeycomb structure is shown in Fig.(6).

4.1.3. Optimisation methodology

Since there exists no known analytical solution to the present problem, a numerical optimisation procedure must be found which minimises the total number of simulations and yields simple design criteria to suit different engineering requirements on thermal performance. To reduce the number of simulations, the cell size has been made uniform, and the resulting optimal geometry can subsequently be refined by allowing each cell size to deviate from the uniform value. Only the uniform case is addressed in this paper. The number of cells is then varied from $N = 1$ to its maximum value

$$N_{max} = \frac{D_h - t}{h_{min} + t} \tag{28}$$

where $h_{min} = 2$mm is the minimum cell size value, giving $N_{max} = \{5, 10, 20, 30\}$ for the investigated honeycomb sizes. However to meet the optimal geometry criterion (Eq.(30) below), smaller cell sizes must be considered. Design criteria are formulated in terms of the size ratio (thereafter SR), defined by

$$S_R = \frac{h + t}{D_h} = \frac{1 - t/D_h}{N} \Big(\simeq \frac{1}{N} \text{ for } t \ll D_h \Big) \tag{29}$$

The effect on k_{eq} of adding an extra cell can be to either increase it if conductive transfers are enhanced more than radiative transfers are inhibited, or to decrease it otherwise. Which way it goes is determined by the ratio of radiative to conductive transfers and the degree of rarefaction within the cells, which depends on the cell size. For a high number of cells N (*i.e* small cells), the gaseous resistance to conduction is very large, so much so that for high enough radiation levels, adding an extra cell is expected to reduce k_{eq} by further inhibiting radiative transfers without affecting conduction. As a consequence, the optimal size ratio S_R^* is defined as that beyond which adding an extra cell would result in a k_{eq} drop lower than a predefined threshold α. Mathematically, this translates as

$$-\alpha \leq \frac{k_{eq,N^*+1} - k_{eq,N^*}}{k_{eq,N^*}} \leq 0 \iff -\alpha \leq \frac{Q_{N^*+1} - Q_{N^*}}{Q_{N^*}} \leq 0 \tag{30}$$

where N^* is the number of cells at optimal size ratio. The objective of this study is to express S_R^* in terms of a dimensionless number N_{rc}; $S_R^* = f(N_{rc})$. As aforementioned, N_{rc} may quantify the ratio of conductive to radiative transfers where only one cell is present:

$$N_{rc} = \left| \frac{Q_{rad}}{Q_{cond}} \right| \Big)_{1 \text{ cell}} \tag{31}$$

Assuming infinite gaseous resistance to conduction through the cells, we have, for opaque materials and per unit depth

$$\begin{aligned} |Q_{cond}|)_{1\text{ cell}} &\approx \frac{2t < k_s > (T_h - T_c)}{D_h} \\ |Q_{rad}|)_{1\text{ cell}} &\approx \frac{\sigma(T_h^4 - T_c^4)(D_h - 2t)}{1/\epsilon(T_c) + 1/\epsilon(T_h) + \sqrt{2} - 1} \end{aligned} \tag{32}$$

where $2t$ is the total column width over which conduction takes place in the solid, $< k_s >$ is the solid thermal conductivity averaged between T_c and T_h, σ is Stefan's constant, ϵ is the Planck-averaged emissivity, and the denominator of the second line is the radiative resistance between the hot and cold surfaces. Combining Eqs.(31,32), we get

$$N_{rc} = \sigma \frac{1/ < k_s >}{1/\epsilon(T_h) + 1/\epsilon(T_c) + \sqrt{2} - 1} \frac{(D_h - 2t)D_h}{2t} \frac{T_h^4 - T_c^4}{T_h - T_c} \tag{33}$$

This definition of N_{rc} is used throughout the remainder of this paper. Its adaptation for semi-transparent materials is discussed in Appendix B.

4.2. Design tool 1: $S_R{}^*$

4.2.1. Analytical study

The dependence of S_R^* on N_{rc} can be estimated analytically with a few approximations. The full derivation, detailed in Appendix C, leads to

$$-\alpha \leq \frac{\Delta Q_N}{Q_N} \simeq \frac{\frac{<k_g> D_h (D_h - 2t)}{2 <k_s> h_N h_{N+1}} - N_{rc}}{N(N+1)(1 + \frac{N_{rc}}{N})} \leq 0 \tag{34}$$

where $\Delta Q_N = Q_{N+1} - Q_N$, $< k_g >$ is the temperature-averaged gaseous conductivity, and h_N is the cell size for N cells. The first term in the numerator represents the increase in conductive transfer by the addition of an extra cell whereas the second term represents the decrease in radiative transfer. As such, Eq.(34) illustrates the relationship between conductive and radiative transfers: at high radiation levels ($N_{rc} \gg 1$), $\Delta Q_N/Q_N$ is negative *for all N*, and as many cells as possible must be used. When $N_{rc} \ll 1$ however, $\Delta Q_N/Q_N$ can be positive and the number of cells has to be limited.

The positive root of Eq.(34) is (see Appendix C)

$$N^* = \frac{1 + N_{rc}}{2} \left(-1 + \sqrt{1 + \frac{4N_{rc}(\frac{1}{\alpha} - 1)}{(1 + N_{rc})^2}} \right) \tag{35}$$

Insofar as $N \leq N_{max} = D_h/t - 1$ for h to remain positive, any value of $N \geq N^*$ will satisfy Eq.(34). This yields a condition on α:

$$\alpha > \frac{1}{1 + (\frac{D_h}{t} - 1)(1 + \frac{D_h}{tN_{rc}})} \tag{36}$$

which, for the present work, gives $\alpha > 3 \cdot 10^{-4}$. A value of α=0.001=0.1% is used for the remainder of this work, which allows for a Taylor expansion of the square root term of Eq.(35), leading to a greatly simplified form

$$\begin{aligned} N^* \simeq \sqrt{\frac{N_{rc}}{\alpha}} &\iff S_R^* \simeq (1 - \frac{t}{D_h})\sqrt{\frac{\alpha}{N_{rc}}} \ (\alpha \ll 1) \\ &\iff S_R^* \simeq \sqrt{\frac{\alpha}{N_{rc}}} \ (\alpha \ll 1 \ \& \ t \ll D_h) \end{aligned} \tag{37}$$

which constitutes a simple design criterion and will be shown to be valid in the next section with the introduction of a multiplying factor. No scale effects appear in this result in the $t \ll D_h$ limit; this is because scale effects would only arise from conduction effects, which have been neglected, or from radiation propagation in semi-transparent solids, which has been incorporated in N_{rc} (see Appendix B). Besides, note that since $N_{rc} \propto D_h^2$ for $t \ll D_h$, we have $N^* \propto D_h$ and so $S_R^* \propto 1/D_h$. Recalling the definitions of S_R (Eq.(29)) and N_{rc} (Eq.(33)), we get that h^* is independent of D_h:

$$h^* + t = \sqrt{\frac{2\alpha t < k_s >}{(T_h^2 + T_c^2)(T_h + T_c)} \frac{1/\epsilon(T_h) + 1/\epsilon(T_c) + \sqrt{2} - 1}{\sigma}} \tag{38}$$

and only depends on the wall thickness, temperature and materials' properties, but not on the system size, which is a remarkable result.

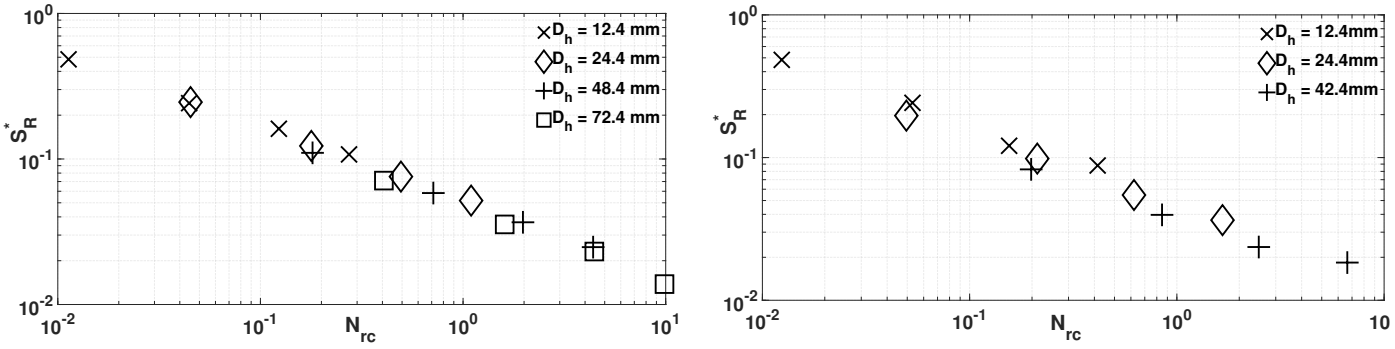

(a) ss321

(b) alumina

Figure 7: Numerical results for S_R^* as a function of N_{rc} for ss321 and alumina. A logarithmic scale is used on both axes.

4.2.2. Numerical results

The numerical results for S_R^* as a function of N_{rc} for ss321 and alumina are plotted in Figs.(7a,7b). As anticipated, the scatter in the data between different sizes is minimal for ss321 and decreases with increasing N_{rc}, which is consistent with the observation of the previous section that Eq.(34) predicts scale effects in opaque media to arise from conductive effects only. However for alumina some scatter is visible, which is attributed to its semi-transparency (see below). But in both cases, all points seem to align on a straight line, suggesting a power-law relationship between S_R^* and N_{rc}. Consequently, the points were fitted to a square-root law of the form $S_R^* = A\sqrt{\alpha/N_{rc}}$ for all sizes independently, and for all points taken together. To further test the square-root law, a power-law fit was additionally tested with an unconstrained power exponent, $S_R^* = A(\alpha/N_{rc})^B$. The results for both are shown in Table 1.

For all sizes, the r^2 coefficients for both fit types exceed 0.995, the unconstrained power exponents are very close to 0.5 (with a deviation lower than 1.3% in five cases), and the multiplying factors have similar amplitudes as those of the square-root fits. These results confirm the validity of the square-root law predicted by Eq.(37) for a given scale. The case where all points are fitted together is different. For ss321, there is perfect agreement between both fits, suggesting both that scale effects are insignificant, and that the square-root law, which was derived from physical considerations, is valid with high accuracy - provided a multiplying constant is added. For alumina, both fits are of a lesser quality, with r^2 coefficients of order 0.98. This indicates the presence of scale effects (which goes together with the noticeable presence of data scatter in Fig.(7b) as noted above) and is a first important difference between opaque and semi-transparent solid media: because the latter participate in radiative transfers through internal volume mechanisms, the radiative fluxes depend on the amount of solid volume, just like conductive fluxes do, and a fit which does not account for scale effects is of lesser quality. Also, it is important to note that the unconstrained power law fit yields a larger power exponent of 0.5588 for alumina due to its semi-transparency, which indicates that the tweak to N_{rc} for semi-transparent media suggested in Appendix B together with the model of Appendix C is incomplete and needs some refinement to incorporate scale effects for non-opaque media.

The presence of a multiplying constant larger than unity suggests an overestimation of the radiative flows in the analytical model of section 4.2.1, and is attributed to the one-dimensional radiative flow assumption, which underestimates the efficiency of the two-dimensional radiative barrier structure. In practice radiative flows are two-dimensional, allowing some radiative energy to be either absorbed on the sides or reflected back towards the hot sur-

Table 1: Square root and power law fits for S_R^* for ss321 and alumina optimisation

		Square root fit	**Power law fit**
SS321	D_h=12.4mm	$S_R^* = 1.640\sqrt{\frac{\alpha}{N_{rc}}}$, $r^2 = 0.9965$	$S_R^* = 1.528(\frac{\alpha}{N_{rc}})^{0.4759}$, $r^2 = 0.9975$
	D_h=24.4mm	$S_R^* = 1.655\sqrt{\frac{\alpha}{N_{rc}}}$, $r^2 = 0.9998$	$S_R^* = 1.619(\frac{\alpha}{N_{rc}})^{0.4949}$, $r^2 = 0.9997$
	D_h=48.4mm	$S_R^* = 1.510\sqrt{\frac{\alpha}{N_{rc}}}$, $r^2 = 0.9955$	$S_R^* = 1.226(\frac{\alpha}{N_{rc}})^{0.4635}$, $r^2 = 0.9999$
	D_h=72.4mm	$S_R^* = 1.436\sqrt{\frac{\alpha}{N_{rc}}}$, $r^2 = 0.9984$	$S_R^* = 1.377(\frac{\alpha}{N_{rc}})^{0.4935}$, $r^2 = 0.9977$
	All points	$S_R^* = 1.632\sqrt{\frac{\alpha}{N_{rc}}}$, $r^2 = 0.9974$	$S_R^* = 1.628(\frac{\alpha}{N_{rc}})^{0.4993}$, $r^2 = 0.9972$
Alumina	D_h=12.4mm	$S_R^* = 1.704\sqrt{\frac{\alpha}{N_{rc}}}$, $r^2 = 0.9966$	$S_R^* = 1.736(\frac{\alpha}{N_{rc}})^{0.5062}$, $r^2 = 0.9950$
	D_h=24.4mm	$S_R^* = 1.393\sqrt{\frac{\alpha}{N_{rc}}}$, $r^2 = 0.9990$	$S_R^* = 1.328(\frac{\alpha}{N_{rc}})^{0.4891}$, $r^2 = 0.9990$
	D_h=48.4mm	$S_R^* = 1.164\sqrt{\frac{\alpha}{N_{rc}}}$, $r^2 = 0.9997$	$S_R^* = 1.131(\frac{\alpha}{N_{rc}})^{0.4951}$, $r^2 = 0.9997$
	All points	$S_R^* = 1.619\sqrt{\frac{\alpha}{N_{rc}}}$, $r^2 = 0.9798$	$S_R^* = 1.972(\frac{\alpha}{N_{rc}})^{0.5588}$, $r^2 = 0.9869$

face., resulting in lower energy flows to the cavities bottom wall than assumed in the calculations and therefore higher values for S_R^*, hence a constant larger than unity. Finally, the fact that these constants generally decrease with increasing scales illustrates the presence of the well-known thermal coupling between conduction and radiation and is seen to be more pronounced for alumina. This shows that because they participate in thermal radiation, semi-transparent media exhibit larger thermal coupling, which is a second fundamental difference between the two types of materials.

All together, the above results suggest a law of the form

$$\begin{cases} S_R^* = 1.632\sqrt{\frac{\alpha}{N_{rc}}} & \text{for ss321 } (\mathrm{r}^2 = 0.9974) \\ S_R^* = 1.972\left(\frac{\alpha}{N_{rc}}\right)^{0.56} & \text{for alumina } (\mathrm{r}^2 = 0.9869) \end{cases} \tag{39}$$

can be used for designing and engineering purposes with high accuracy.

4.3. Design tool 2: k_{eq}

4.3.1. Analytical study

An analytical expression for k_{eq} can be derived in the same way as S_R^*. The full derivation, given in Appendix C, leads to

$$k_{eq} \simeq \frac{2t < k_s >}{D_h}\left(1 + \frac{N_{rc}}{N}\right) + \frac{< k_g >}{1 - (N+1)t/D_h} \tag{40}$$

which can be expressed in terms of S_R using Eq.(29), and simplified at optimal geometry using Eq.(39). Also, it must be remembered that $< k_g >$ is a function of the cell size and therefore of N.

It emerges from Eq.(40) that the effects of radiation manifest solely through the N_{rc}/N term, which implies that the radiative contribution to k_{eq} can be expressed as a fraction of the solid conduction contribution; for example if $N_{rc}/N = 0.5$, conduction is twice as high as radiation in magnitude (only approximately because of the presence of the gaseous term but whose amplitude is small). A consequence of this result is that N_{rc} is not only an evaluation of the single-cell radiation to conduction ratio, but is also interpreted as a critical number of cells which allows to determine which transfer mode predominates:

$$\begin{cases} N < N_{rc} \Rightarrow \text{ Radiation predominates} \\ N = N_{rc} \Rightarrow \text{ Conduction} \simeq \text{Radiation} \\ N > N_{rc} \Rightarrow \text{ Conduction predominates} \end{cases} \tag{41}$$

Interestingly, this implies that the number of cells required to lower the magnitude of radiative transport below that of conduction is equal to N_{rc}; for example if $N_{rc} = 5$, it takes 5 cells for conduction to become predominant (for a fixed D_h). Therefore, the sole knowledge of N_{rc} is enough to

know how many cells are required to negate the effects of radiation, which conveniently complements the S_R^* based design tool of the previous section; for $N \gg N_{rc}$, the energy transfer within the honeycomb is almost reduced to pure conduction. Equations (39,40) thus emerge as two practical design tools.

Besides, it is interesting to note that for $N \gg N_{rc}$ or $N = N^*$, the scale dependency of k_{eq} is imposed by conductive transport, and k_{eq} and D_h obey an inverse power law. In the former case, it is because the N_{rc}/N term vanishes in Eq.(40). In the latter, it arises from the fact that $N^* \propto \sqrt{N_{rc}} \propto D_h$ for $t \ll D_h$. In both cases, k_{eq} decreases linearly with increasing system size - this effect is exploited in section 4.4 below. But in the general case, the scale dependency of k_{eq} can be written as $1/D_h + AD_h/N$ where A is defined by $N_{rc} = AD_h^2$ for $t \ll D_h$. A study of the derivative of this term reveals that N_{rc} again appears as a critical number:

$$\begin{cases} N < N_{rc} \Rightarrow \frac{\partial k_{eq}}{\partial D_h} > 0\text{: } k_{eq} \text{ increases with } D_h \\ N \geq N_{rc} \Rightarrow \frac{\partial k_{eq}}{\partial D_h} < 0\text{, } k_{eq} \text{ decreases with } D_h \end{cases} \quad (42)$$

This is coherent with the interpretation of N_{rc} (Eq.(41)); when $N < N_{rc}$, radiation predominates and as such its scale dependency ($\propto D_h^2$) prevails over the conduction one ($\propto 1/D_h$), resulting in an overall increase of k_{eq} with D_h, and vice-versa.

From the above results, it emerges that all the relevant thermal properties and design criteria of a square-angle cell square honeycomb can be predicted from the knowledge of the non-dimensional number N_{rc} which only depends on the temperature, material properties and geometry of the honeycomb. N_{rc} is therefore a useful dimensionless number for the thermal study and design of honeycombs which avoids complex numerical simulations. However, for those cases where there exist lateral losses, the losses would have to be assessed and their contribution to the global energy flow added to Eq.(40); from there a similar equation to Eq.(34) can be obtained, leading to another form for the $S_R^* = f(N_{rc})$ function.

4.3.2. Numerical results

The analytical predictions for k_{eq}^* from Eq.(40) are compared to numerical results in Figs.(8a,8b) for ss321 and alumina at optimal geometries. The agreement between analytical predictions and numerical results is very good in all cases, and improves with larger sizes. For ss321, at the two smallest scales, Eq.(40) underestimates k_{eq}^* by factors between 0.75% and 8.63%, while at the largest two scales, the differences vary between -3.49% and 5.32%. Besides, note that for larger scales and higher temperatures (*i.e* for larger N_{rc} values), the analytical predictions become overestimations of k_{eq}^*. For alumina however, the predictions remain underestimations at all temperatures and scales, with differences not exceeding 7.7%, 7.4% and 4.1% in order of increasing scale, and are of the same order as for ss321. However, the fact that Eq.(40) underestimates k_{eq} for all scales and temperatures for alumina is attributed to a larger thermal coupling (see section 4.2.2) which is not accounted for in the analytical predictions. These results validate Eq.(40) for ss321 (resp. alumina) for temperatures up to 1600K (resp. 1200K) and N_{rc} values up to 10 with an accuracy better than 8.63% (resp. 7.7%) in magnitude.

One additional comment can be made. As T_h increases, k_{eq} increases for ss321 but decreases for alumina. This directly reflects the solid conductivity temperature dependency in both cases since at optimal geometry (and beyond), Eq.(40) reduces to $k_{eq} = 2t < k_s > /D_h$. This highlights the crucial role played by solid conductivity in the design of high-temperature honeycomb thermal insulators, of which an example is given in the next section.

4.4. Application to high-temperature thermal insulation

We now apply the above results to the design and optimisation of high-temperature thermal insulation, where the thermal resistances of honeycomb structures and ceramic fibre insulation (therafter CFI) of the same

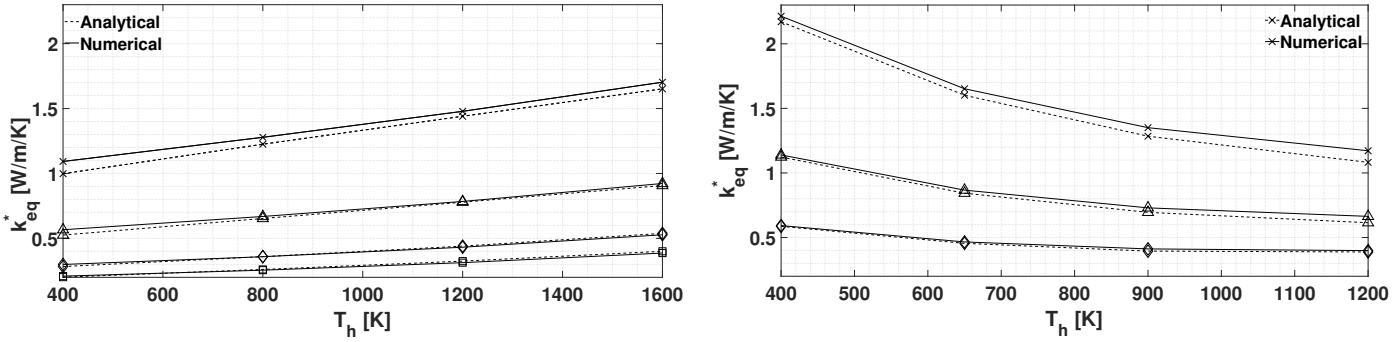

(a) ss321

(b) alumina

Figure 8: Comparison of k_{eq} numerical results (solid lines) and predictions from Eq.(40) (dashed lines) at optimal geometry for ss321 and alunmina for D_h=12.4mm (cross markers), D_h=24.4mm (triangle markers), D_h=48.4mm (diamond markers) and D_h=72.4mm (square markers).

size are compared. Here, because the structures are square, comparing the thermal resistances is equivalent to comparing the thermal conductivities (which are scale-dependent for honeycombs). Equation (40) will be used for honeycombs, and data reported in Ref.[7] is used for CFI.

In Eq.(40), it can be seen that the key parameters to honeycomb thermal efficiency are k_s, D_h, P, N, t and N_{rc}. The effect of the first four are obvious from Eq.(40); structures with the lowest solid thermal conductivity, largest sizes, lowest pressures and the largest feasible number of cells must be sought. As for N_{rc}, its contribution is negligible when $N \gg N_{rc}$. The main parameters on which N_{rc} depends are the material's emissivity, t and D_h. As a consequence, if N is large enough, the emissivity is not a parameter of interest - but D_h and t are, as they appear outside N_{rc} in Eq.(40).

Opaque solid materials are considered first. In view of the above, five values of D_h (100, 200, 300, 400 and 500 mm) and two values of P (0.1 and 10 Pa) are considered. The wall thickness t will be lowered until acceptable thermal performance is reached, and N is set so that $h = t$, which also ensures that $N = (D_h/t - 1)/2 \gg N_{rc}$. Different solid materials are considered to vary k_s.

Results for ss321 are presented in Figs.(9a-9f) for wall thicknesses t=$\{100,\ 50,\ 10\}\mu$m. It is seen that with a thickness of 100μm and a pressure of 10Pa, only the largest sizes outperform CFI above a certain temperature threshold which decreases for P=0.1Pa. Reducing t down to 50μm lowers the temperature threshold and allows more sizes to outperform CFI for a wider range of temperatures; for P=10Pa (resp. 0.1Pa), this happens for all sizes above T_h = 1000K (resp. T_h = 900K). These results are satisfactory since this work is concerned with high-temperature insulation. However, the most interesting results are obtained by further reducing t down to 10μm, in which case all tested sizes significantly outperform CFI for all temperatures. At 10Pa, the honeycomb conductivities at 1600K range from 0.0022W/m/K (D_h = 500mm) to 0.0078W/m/K (D_h = 100mm). At room temperature (300K), these numbers become 0.0012W/m/K (resp. 0.0045W/m/K). At 0.1Pa, they are 0.0017W/m/K (resp. 0.0073W/m/K) at 1600K, and 0.00058W/m/K (resp. 0.0039W/m/K) at room temperature. Note that these room temperature values are even smaller than those reported for VIP's at the same temperature, at both 0.1Pa and 10Pa [5, 6]. Besides, another advantageous distinctive feature of honeycombs is that the temperature dependency of k_{eq} is much weaker than for CFI. This is because with $N \gg N_{rc}$, the temperature dependency of k_{eq} is only due to that of $< k_s >$. For CFI however, the temperature dependency is mainly caused by increased

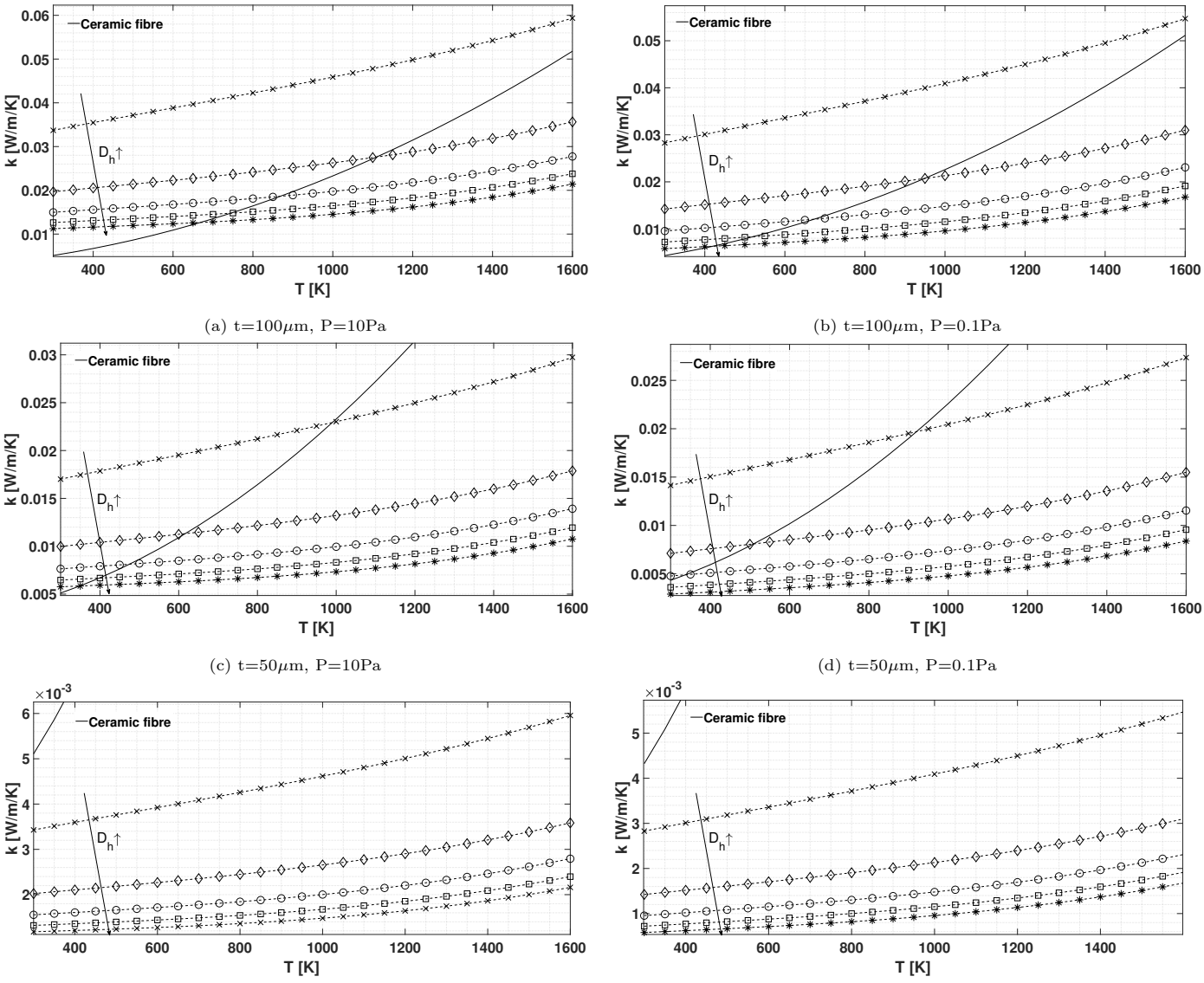

(a) t=100μm, P=10Pa

(b) t=100μm, P=0.1Pa

(c) t=50μm, P=10Pa

(d) t=50μm, P=0.1Pa

(e) t=10μm, P=10Pa

(f) t=10μm, P=0.1Pa

Figure 9: Thermal conductivity comparison between ss321 honeycombs and CFI for several values of wall thickness t and pressure P. The honeycomb sizes are D_h = 100mm (cross markers), 200mm (diamond markers), 300mm (round markers), 400mm (square markers), and 500mm (star markers), indicated in increasing order on the graphs.

radiative transfers at higher temperatures. This difference in behaviour is further illustrated below.

These results show that ss321 honeycombs exhibit lower thermal conductivities than CFI at all temperatures for wall thicknesses $t \leq 10\mu$m. In an attempt to ease this thickness requirement, other solid materials are sought which have a lower thermal conductivity. Most materials which are opaque to thermal radiation for layers as thin as 10μm and high enough melting points are metals. Of all known pure metals only bismuth, manganese, plutonium and mercury have a lower conductivity that stainless steel. But plutonium is radioactive, and the melting points of mercury, manganese and bismuth are too low. However a few alloys display lower thermal conductivities than ss321 of which a titanium alloy, Ti-6Al-4V, has the lowest conductivity of about 7 W/m/K at room temperature and a melting point of about 1873K, and is therefore a good candidate. Temperature-dependent values for its thermal conductivity and emissivity were found in Boivineau et al. [59] and González-Fernández et al. [60] (the reported data shows a negligible temperature dependency of its emissivity). The results are presented in Figs.(10a-10b) and show that similar thermal performance is achieved as with a 10μm ss321 wall; at $P = 0.1$Pa, all sizes outperform CFI for all temperatures, while at $P = 10$Pa, there remains a temperature threshold of $T_h = 500$K only for $D_h = 100$mm. At this pressure, the honeycomb conductivities range from 0.0071W/m/K ($D_h = 500$mm) to 0.017W/m/K ($D_h = 100$mm) at 1600K, and from 0.0038W/m/K ($D_h - 500$mm) to 0.0072W/m/K ($D_h = 100$mm) at 300K.

The full potential of honeycombs is best illustrated in Figs.(11a-11b) where the ratios of CFI to honeycomb conductivities are shown for 10μm ss321 and 50μm titanium alloy honeycombs. In all cases, the ratio increases with increasing temperatures: the higher the temperature, the larger the thermal gain honeycombs offer over CFI. This is a direct consequence of the above remark on the CFI and honeycomb conductivities temperature dependencies. At a pressure of 10Pa, the 10μm ss321 honeycomb boasts conductivities 3.5 (resp. 14.9) times lower than CFI at 300K (resp 1600K) for $D_h = 100$mm. For $D_h = 500$mm, these numbers become 6.5 (resp. 36). Lowering the pressure down to 0.1Pa drives these ratios up to even higher values. The 50μm titanium alloy honeycomb displays a lower efficiency; for $P = 10$Pa, the ratios range from 0.71 (300K) to 2.99 (1600K) for $D_h = 100$mm, and fall between 1.35 (300K) and 7.25 (1600K) for $D_h = 500$mm (these ratios also go up with lower pressures).

A ratio lower than unity indicates that the CFI achieves a better performance - however it is only observed for $D_h = 100$mm and $T_h \leq 500$K. But the 50μm value was chosen to ease the restriction on t; a 10μm titanium alloy honeycomb would show even greater efficiency than its ss321 counterpart. What is important to note is that all these results demonstrate the capacity of honeycombs to surpass existing ultra-high temperature insulation technologies in terms of thermal performance; for example, a thickness of 50μm (roughly that of commercially available metal foils) of this titanium alloy would suffice to outperform CFI over the whole range of operating temperatures.

Note that both ss321 and Ti-6Al-4V have been studied below their melting points (around 1670K for ss321 and 1930K for Ti-6Al-4V) but past their usual maximum service temperature (about 1180K for ss321, and 780K for titanium alloy Ti-6Al-4V) above which they loose a significant part of their structural strength. However they have been shown to outperform CFI at all studied temperatures which illustrates their efficiency across their respective operating temperature ranges, and highlights their potential at higher temperatures for applications where no structural strength is required or where structural reinforcement is achievable.

As a comparison, equivalent conductivities for alumina

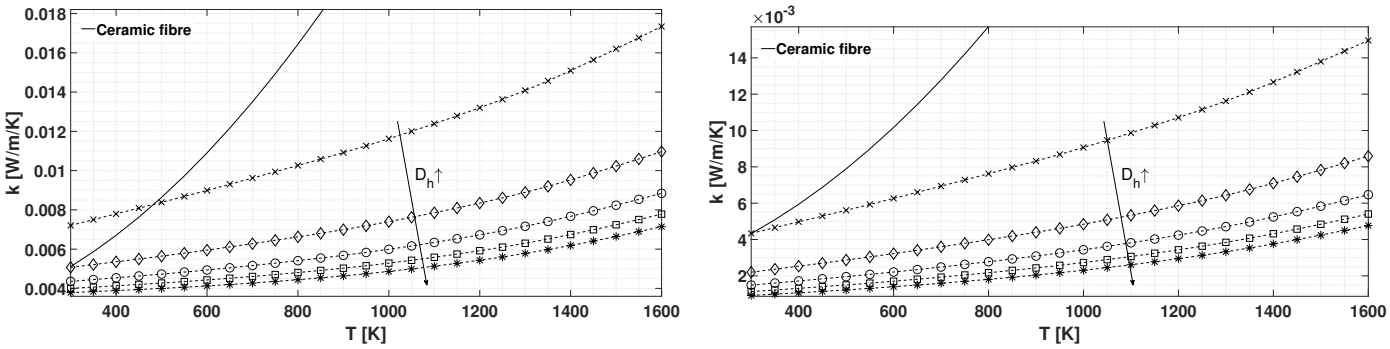

(a) t=50μm, P=10Pa (b) t=50μm, P=0.1Pa

Figure 10: Thermal conductivity comparison between titanium honeycombs and CFI for $t = 50\mu$m and two P values. The honeycomb sizes are $D_h = 100$mm (cross markers), 200mm (diamond markers), 300mm (round markers), 400mm (square markers), and 500mm (star markers), indicated in increasing order on the graphs.

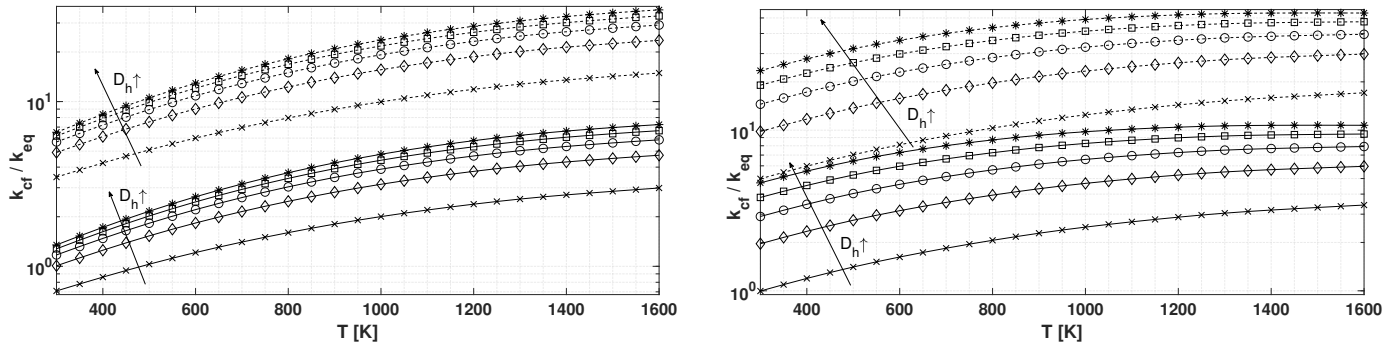

(a) P=10Pa (b) P=0.1Pa

Figure 11: Ratio of ceramic fibre to honeycomb conductivities at t=50μm (titanium alloy, solid lines) and t=10μm (ss321, dashed lines) for two pressures and all sizes $D_h = 100$mm (cross markers), 200mm (diamond markers), 300mm (round markers), 400mm (square markers), and 500mm (star markers), indicated in increasing order on the graphs. A logarithmic scale is used for the vertical axis.

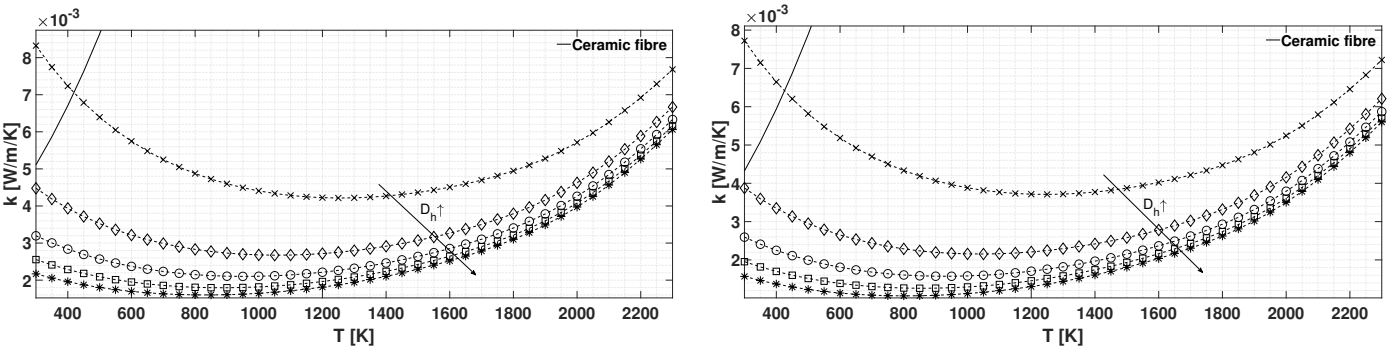

(a) t=10μm, P=10Pa (b) t=10μm, P=0.1Pa

Figure 12: Thermal conductivity comparison between alumina honeycombs and CFI for $t = 10\mu$m and two P values. The honeycomb sizes are $D_h = 100$mm (cross markers), 200mm (diamond markers), 300mm (round markers), 400mm (square markers), and 500mm (star markers), indicated in increasing order on the graphs. Note that ceramic fibre is off the scale for most of the graph.

honeycombs with $t = 10\mu$m are shown in Figs.(12a,12b) for temperatures up to alumina's melting point (2345K). It is seen that alumina ceramics also outperforms CFI for all scales and temperatures - albeit with a threshold of about 450K for the lowest scale. k_{eq} values are similar to the 50μm titanium alloy honeycomb: at 1600K and 10Pa for example, they are 0.0077 (resp. 0.0061) W/m/K for $D_h = 100$mm (resp. $D_h = 500$mm). At 300K, they become 0.0083 (resp. 0.0022) W/m/K. These values, which go down at 0.1Pa, show that ceramics honeycombs, although not as thermally efficient as metal ones, retain low conductivities (<0.01W/m/K) up to their melting point. This allows to raise the maximum service temperature of currently commercially available high-temperature insulation, which is crucial for the development of UHTS technologies, among other high-temperature applications.

Finally, differences between opaque and semi-transparent materials manifest once more on Figs.(12a,12b) in the shape of the curves, which have a u-shape for alumina; the initial low temperature decrease caused by its thermal conductivity is outweighed at higher temperatures by the increase of N_{rc}. The fact that N_{Rc} still contributes to k_{eq} even with such small cells illustrates the fact that radiation levels are higher in semi-transparent materials and consequently even smaller cells would be needed for k_{eq} to keep decreasing at higher temperatures.

All the results in this section demonstrate the potential of thin-walled honeycomb structures to both outperform existing high-temperature insulation technologies, and to raise its maximum service temperature whilst retaining good thermal performance, and provide motivation for research into the development of manufacturing processes for such structures.

5. Summary and future work

In this paper, a theoretical and numerical models are presented for the modelling of combined conductive and radiative thermal energy transfers in opaque or semi-transparent cuboid multi-media structures containing obstacles and internal boundaries. Grid independence is then established along with a 2D/3D convergence which allows to carry out the rest of the study in 2D.

The model is subsequently applied to the design of high-temperature thermal insulators based on honeycomb geometries. First, a numerical optimisation methodology is established, and a dimensionless number N_{rc} is defined. Then, analytical expressions are derived for the honeycomb equivalent conductivity k_{eq} and the $S_R^* = f(N_{rc})$ function, where S_R^* is the optimal size ratio. A study of both equations is presented, during which much insight is gained into the behaviour of energy transfers in honeycombs. The analytical results are then compared to numerical results. In particular, key findings include:

- N_{rc}, defined by Eq.(33) as the ratio of radiation to conduction levels at one cell, allows to know which transfer mode dominates depending on the number of cells, and how many cells are required to negate radiative transfers. It also appears in the expression for the equivalent conductivity.
- The analytical predictions for S_R^* (Eq.(37)) are validated for ss321, provided a multiplying constant is added for S_R^*. Good agreement is also shown for alumina, although the power exponent is found to be slightly larger than predicted (0.56 instead of 0.5) due to scale effects. Following this study, a first engineering design criterion is established (Eq.(39)).
- The analytical predictions for k_{eq} show a maximum deviation from numerical results of 8%, and generally overestimate k_{eq} for ss321 and underestimate it for alumina.
- Fundamental differences were highlighted between opaque and semi-transparent materials; mainly that semi-transparent materials show larger scale effects and a larger thermal coupling between conductive and radiative transfers.

- Finally, it was shown that thin walled metal honeycombs (*e.g* 10μm ss321 or 50μm titanium alloy) have the potential to significantly outperform currently available high-temperature thermal insulation (like ceramic fibre insulation) with, for example, thermal conductivities below 0.008W/m/K at 1600K and 10Pa. Additionally, thin-walled alumina ceramics honeycomb, whilst less efficient, also allow an improvement on currently available technologies and, crucially, allow to raise the current maximum service temperature of insulation technologies by retaining thermal conductivities below 0.01W/m/K up to their melting point. These results provide a good basis to motivate research into the development of manufacturing processes of such structures.

Further areas of investigation may include:

- Refining the model presented in Appendix C for semi-transparent materials.
- The development of processes allowing the manufacture of thin-walled structures such as those of section 4.4 has been showed to be of great importance.

References

[1] M. Lott, S.-I. Kim, C. Tam, D. Elzinga, S. Heinen, L. Munuera, U. Remme, Technology roadmap: Energy storage, Tech. rep., International Energy Agency (March 2014).

[2] A. Robinson, Ultra-high temperature thermal energy storage. Part 1: Concepts, Journal of Energy Storage Vol. 13 (2017) pp. 277–286. doi:10.1016/j.est.2017.07.0202.

[3] A. Robinson, Ultra-high temperature thermal energy storage. Part 2: Engineering and operation, Journal of Energy Storage 18 (2018) 333–339. doi:10.1016/j.est.2018.03.013.

[4] A. Datas, A. Ramos, A. Martí, C. del Cañizo, A. Luque, Ultra high temperature latent heat energy storage and thermophotovoltaic energy conversion, Energy 107 (2016) 542–549. doi:http://dx.doi.org/10.1016/j.energy.2016.04.048.

[5] R. Baetens, B. P. Jelle, J. V. Thue, M. J. Tenpierik, S. Grynning, S. Uvsløkk, A. Gustavsen, Vaccum Insulation Panels for building applications: A review and beyond, Energy and Buildings 42 (2010) 147–173. doi:10.1016/j.enbuild.2009.09.005.

[6] A. Lorenzati, S. Fantucci, A. Capozzoli, M. Perino, VIPs thermal conductivity measurement: test methods, limits and uncertainty, Energy Procedia 78 (2015) 418–423. doi:10.1016/j.egypro.2015.11.686.

[7] K. Daryabeigi, G. R. Cunnigton, J. R. Knutson, Measurement of heat transfer in unbounded silica fibrous insulation and comparison with theory, in: the proceedings of the 29^{th} International thermal conductivity conference, ITCC29, 2008.

[8] J. T. Bevans, R. V. Dunkle, Radiation interchange within an enclosure. Part 1: Absorption and emission behaviour of gases, Journal of Heat Transfer 82 (1) (1960) 1–19. doi:10.1115/1.3679870.

[9] J. T. Bevans, D. K. Edwards, Radiation exchange in an enclosure with directional wall properties, ASME Journal of Heat Transfer 87 (3) (1965) 388–396. doi:10.1115/1.3689121.

[10] J. R. Schornhorst, R. Viskanta, Effect of direction and wavelength dependent surface properties on radiant heat transfer, AIAA Journal 6 (8) (1968) 1450–1455. doi:10.2514/3.4787.

[11] P. M. Engstrom, R. Viskanta, J. S. Toor, Study of radiation interchange in an enclosure consisting of plane isothermal and adiabatic surfaces, Wärme- und Stoffübertragung 3 (2) (1970) 63–69. doi:10.1007/BF01108026.

[12] C. Tien, W. Yuen, Radiation characteristics of honeycomb solar collectors, International Journal of Heat and Mass Transfer 18 (12) (1975) 1409–1413. doi:10.1016/0017-9310(75)90254-9.

[13] J. T. Bevans, Radiant heat-transfer analysis of a furnace or other combustion enclosure, Journal of Heat Transfer 83 (2) (1961) 226–232. doi:10.1115/1.3680527.

[14] K. G. T. Hollands, Honeycomb devices in flat-plate solar collectors, Solar Energy 9 (3) (1965) 159–164.

[15] E. Sparrow, P. Kruger, R. Heinisch, Radiation from cavities with nonisothermal heat conducting walls, Journal of Heat Transfer 96 (1) (1974) 15–20. doi:10.1115/1.3450132.

[16] K. G. T. Hollands, G. D. Raithby, F. B. Russel, R. G. Wilkinson, Coupled radiative and conductive heat transfer across honeycomb panels and through single cells, International Journal of Heat and Mass Transfer 27 (11) (1984) 2119–2131. doi:10.1016/0017-9310(84)90199-6.

[17] C. L. Ten, P. S. Jagannathan, B. F. Armaly, Analysis of lateral conduction and radiation along two parallel long plates, AIAA Journal 7 (9) (1969) 1806–1808. doi:10.2514/3.5400.

[18] W. Platzer, Calculation procedure for collectors with a honeycomb cover of rectangular cross-section, Solar Energy 48 (6) (1992) 381–393. doi:10.1016/0038-092X(92)90047-E.

[19] A. Sanchez, T. F. Smith, Surface radiation exchange for two-dimensional rectangular enclosure using the discrete-ordinates method, Journal of Heat Transfer 114 (2) (1992) 465–472. doi:

10.1115/1.2911296.

[20] P. J. Coelho, J. M. Gonçalves, M. G. Carvalho, Modelling of radiative heat transfer in enclosures with obstacles, International Journal of Heat and Mass transfer 41 (4-5) (1998) 745–756. doi:10.1016/S0017-9310(97)00158-0.

[21] D. Lacroix, G. Parent, F. Asllanaj, G. Jeandel, Coupled radiative and conductive heat transfer in a non-grey absorbing and emitting semitransparent media under collimated irradiation, Journal of Quantitative Spectroscopy and Radiative Transfer 75 (5) (2002) 589–609. doi:10.1016/S0022-4073(02)00031-6.

[22] O. Wellele, H. R. B. Orlande, N. Ruperti Jr., M. J. Colaco, A. Delmas, Couple conduction-radiation in semi-transparent materials at high temperatures, Journal of Physics and Chemistry of Solids 67 (2006) 2230–2240. doi:10.1016/j.jpcs.2006.06.007.

[23] F. Asllanaj, G. Jeandel, J. R. Roche, Numerical solution of radiative transfer equation coupled with nonlinear heat conduction equation, International Journal of Numerical Methods for Heat and Fluid Flow 11 (5) (2001) 449–473. doi:10.1108/EUM0000000005528.

[24] H. Kessentini, R. Capdevila, J. Castro, A. Oliva, C. Bouden, Three dimensional heat transfer analysis of combined conduction and radiation in honeycomb transparent insulation, Solar Energy 105 (2014) 58–70. doi:10.1016/j.solener.2014.02.027.

[25] M. Antar, Thermal radiation role in conjugate heat transfer across a multiple-cavity building block, Energy 35 (8) (2010) 3508–3516. doi:10.1016/j.energy.2010.04.055.

[26] M. A. Badri, Y. Favennec, P. Jolivet, B. Rousseau, Conductive-radiative heat transfer within sic-based cellular ceramics at high-temperatures: A discrete-scale finite element analysis, Finite Elements in Analysis and Design 178 (2020). doi:10.1016/j.finel.2020.103410.

[27] K. G. T. Hollands, Natural convection in horizontal thin-walled honeycomb panels, Journal of Heat Transfer (1973) 439–444.

[28] R. L. D. Cane, K. G. T. Hollands, G. D. Raithby, T. E. Unny, Free convection heat transfer across inclined honeycomb panels, Journal of Heat Transfer (1977) 86–91.

[29] P. J. Karditsas, M.-J. Baptiste, Thermal and structural properties of fusion related materials, http://www-ferp.ucsd.edu/LIB/PROPS/PANOS/.

[30] C. Y. Ho, T. K. Chu, Electrical resisitivity and thermal conductivity of nine selected aisi stainless steels, State-of-the-art report, Purdue University, Cindas Report 45 (September 1977).

[31] S. Chapman, T. G. Cowling, The mathematical theory of non-uniform gases, 2nd Edition, Cambridge University Press, 1952.

[32] S. S. Kutateladze, S. Semenovich, Fundamentals of heat transfer, Edwards Arnold Ltd, 1963.

[33] W. M. Rohsenow, J. P. Harnett, Handbook of heat transfer, McGraw-Hill Inc., 1973.

[34] R. W. Barber, D. R. Emerson, Challenges in modeling gas-phase flow in microchannels: from slip to transition, Heat Transfer Engineering 27 (4) (2006) 3–12. doi:10.1080/01457630500522271.

[35] V. K. Michalis, A. N. Kalarakis, E. D. Skouras, V. N. Burganos, Rarefaction effects on gas viscosity in the Knudsen transition regime, Microfluidics and Nanofluidics 9 (4-5) (2010) 847–853. doi:10.1007/s10404-010-0606-3.

[36] A. Beskok, G. E. Karniadakis, Report: A model for flows in channels, pipes, and ducts at micro and nano scales, Microscale Thermophysical Engineering 3 (1) (2010) 43–77. doi:10.1080/108939599199864.

[37] S. M. Hosseini Sarvari, Variable discrete ordinates method for radiation transfer in plane-parallel semi-transparent media with variable refractive index, Journal of Quantitative Spectroscopy and Radiative Transfer 199 (2017) 36–44. doi:10.1016/j.jqsrt.2017.05.018.

[38] J. S. Toor, R. Viskanta, Experiment and analysis of directional effects on radiant heat transfer, Journal of Heat Transfer 94 (November 1972).

[39] J. R. Schornhorst, R. Viskanta, An experimental examination of the validity of the commonly used methods of radiant heat transfer analysis, Journal of Heat Transfer 90 (1968) 1450–1455. doi:10.2514/3.4787.

[40] K. Torrance, E. Sparrow, Biangular reflectance of an electric nonconductor as a function of wavelength and surface roughness, Journal of Heat Transfer 87 (2) (1965). doi:10.1115/1.3689091.

[41] M. F. Modest, Radiative Heat Transfer, 3rd Edition, Academic Press, 2013.

[42] F. Gervais, B. Piriou, Anharmonicity in several polar mode crystals: adjusting phonon self-energy of LO and TO modes in Al_2O_3 and TiO_2 to fit infrared reflectivity, Journal of Physics C: Solid State Physics 7 (1974). doi:10.1088/0022-3719/7/13/017.

[43] F. X. Canning, On Fresnel coefficients for transmission into a lossy medium, 2015 International Conference on Electromagnetics in Advanced Applications (2015). doi:10.1109/ICEAA.2015.7297095.

[44] F. X. Canning, Corrected Fresnel coefficients for lossy materials, 2011 IEEE International Symposium on Antennas and Propagation (APSURSI) (2011). doi:10.1109/APS.2011.5996930.

[45] M. A. Dupertuis, M. Proctor, Generalization of complex snell-descartes and fresnel laws, Journal of the Optical Society of America 11 (1994) 1159–1166. doi:10.1364/josaa.11.001159.

[46] K. E. Oughstrun, C. L. Palombini, Fresnel reflection and transmission coefficients for temporally dispersive attenuative

media, Radio Science 53 (2018) 1382–1397. doi:10.1029/2018RS006646.

[47] J. T. Bevans, D. K. Edwards, Effect of polarization on spacecraft radiation heat transfer, AIAA Journal 3 (7) (1965) 1323–1329. doi:10.2514/3.3131.

[48] J. Batterson, Second order Finite Differences schemes for non-uniform grid spacing, http://fundamentalthinking.blogspot.com/2014/08/second-order-finite-difference-schemes.html (August 2014).

[49] K. Lathrop, Spatial differencing of the transport equation: Positivity vs. Accuracy, Journal of Computational Physics 4 (4) (1969) 475–498. doi:10.1016/0021-9991(69)90015-1.

[50] W. A. Fiveland, The selection of discrete ordinate quadrature sets for anisotropic scattering, Fundamentals of Radiation Heat Transfer 160 (1991) 89–96.

[51] R. Koch, R. Becker, Evaluation of quadrature schemes for the discrete ordiantes method, Journal of Quantitative Spectroscopy and Radiative Transfer 84 (4) (2004) 423–435. doi:10.1016/S0022-4073(03)00260-7.

[52] J. Truelove, Discrete-ordinate solutions of the radiation transport equation, Transactions of the ASME 109 (1987).

[53] W. Fiveland, Discrete-ordinates solutions of the radiative transport equation for rectangular enclosures, Journal of Heat Transfer 106 (4) (1984) 699–706. doi:10.1115/1.3246741.

[54] J. C. Chai, H. S. Lee, S. V. Patankar, Improved treatment of scattering using the discrete ordinates method, Journal of Heat Transfer 116 (3) (1994) 260–263.

[55] G. Colomer, M. Costa, R. Cònsul, A. Oliva, Three-dimensional numerical simulation of convection and radiation in a differentially heated cavity using the discrete ordinates method, International Journal of Heat and Mass Transfer 47 (2) (2004) 257–269. doi:10.1016/S0017-9310(03)00387-9.

[56] S. Thynell, Discrete-ordinates method in radiative heat transfer, International Journal of Engineering Science 36 (1998) 1651–1675. doi:10.1016/S0020-7225(98)00052-4.

[57] J. Donea, S. Giuliani, Finite element analysis of steady-state nonlinear heat transfer problems, Nuclear Engineering and Design 30 (2) (1974) 205–213. doi:10.1016/0029-5493(74)90165-4.

[58] S. V. Patankar, Numerical heat transfer and fluid flow, Washington : Hemisphere Pub. Corp. New York : McGraw-Hill, 1980.

[59] M. Boivineau, C. Cagran, D. Doytier, V. Eyraud, M. H. Nadal, B. Wilthan, G. Pottlacher, Thermophysical properties of solid and liquid Ti-6Al-4V (TA6V) alloy, International journal of thermophysics 27 (2006) 507–529. doi:10.1007/PL00021868.

[60] L. González-Fernández, E. Risueño, R. B. Pérez-Sáez, M. J. Tello, Infrared normal spectral emissivity of Ti-6Al-4V alloy in the 500-1150 K temperature range, Journal of alloys and compounds 541 (2012) 144–149. doi:10.1016/j.jallcom.2012.06.117.

[61] S. Zeidler, T. Posch, H. Mutschke, Optical constants of refractory oxides at high temperatures, Astronomy and Physics 553 (2013). doi:10.1051/0004-6361/201220459.

[62] B. Karlsson, C. G. Ribbing, Optical constants and spectral selectivity of stainless steel and its oxides, Journal of Applied Physics 53 (9) (1982) 6340–6346. doi:10.1063/1.331503.

[63] J. C. Richmond, W. N. Harrison, Total hemispherical emittance of coated and uncoated inconel and types 321 and 430 stainless steel, Journal of Research of the National Bureau of Stadards -C. Engineering and Instrumentation 66C (3) (1962) 261–269.

[64] H. McMahon, Thermal radiation from partially transparent reflecting bodies, Journal of the Optical Society of America 40 (1950). doi:10.1364/josa.40.000376.

[65] L. A. Dombrovsky, J. H. Randrianalisoa, W. Lipiński, D. Baillis, Approximate analytical solution to normal emittance of semi-transparent layer of an absorbing, scattering, and refracting medium, Journal of Quantitative Spectroscopy and Radiative Transfer 112 (2011) 1987–1994. doi:10.1016/j.jqsrt.2011.04.008.

[66] J. Gieseler, A. Adibekyan, C. Monte, J. Hollandt, Apparent emissivity measurement of semi-transparent materials part 2: Theoretical concept, Journal of Quantitative Spectroscopy and Radiative Transfer 258 (2021). doi:10.1016/j.jqsrt.2020.107317.

[67] R. Gardon, The emissivity of transparent materials, Journal of Quantitative Spectroscopy and Radiative Transfer 39 (1956). doi:10.1111/j.1151-2916.1956.tb15833.x.

Appendix A. Optical properties of alumina and ss321

To the authors' knowledge, alumina FPSQ parameters (see section 3.3.2) for the required temperature and spectral ranges have been reported only by Zeidler [61] for wavelengths up to 50μm and temperatures up to 928 K. For the present study, it was assumed that their results applied for wavelengths up to 90μm and temperatures up to 1800K. With these coefficients and Eq.(12), it can be shown that alumina is essentially opaque inside Reststrahlen bands (peaks of reflectance and absorptance, located around 17, 23 and 25 μm for alumina). Outside these bands however, it behaves as a

semi-transparent material for thickness up to ≃0.4 mm for higher energies ($\lambda \leqslant 10\mu m$), and up to 10mm for lower energies ($\lambda \geqslant 30\mu m$). It will therefore be modelled as semi-transparent for all applications considered here.

The attenuation length for thermal radiation within metals is typically a few dozen nanometres, so that ss321 is modelled as opaque. However, available spectral and temperature-dependent data are limited. Karlsson [62] reported values of the optical indices of ss832 (which has a similar composition to ss321) for a very narrow spectral range of $\lambda \in$[0.2-4.8]μm and, to the authors' knowledge, no further data have been published for a wider spectral range and various temperatures. Therefore, total values for the temperature-dependent emissivity [63] together with Kirchhoff's law to obtain the reflectivity will be used.

Appendix B. N_{rc} for semi-transparent materials

The concept of emissivity does not exist for semi-transparent materials. However, "equivalent" emissivities may be defined in various ways depending on a particular situation [41, 64–67]. The following approach is an adaptation of a semi-transparent slab calculation [41, 64] to the particular case of diffuse transmission and reflection defined in the main body of the paper.

Consider a pencil of radiative energy q_{inc} incident from medium 1 upon a slab of thickness d (medium 2) at an array of angles θ_i from the surface normal. Following diffuse reflection, an amount $q_R^{(1)} = \rho_{12}^d q_{inc}$ is reflected towards medium 1, where ρ_{12}^d is the diffuse reflectivity from medium 1 to medium 2. The transmitted intensity is diffuse and equal to $I_t = (1-\rho_{12}^d)q_{inc}/\pi$ in all directions. Therefore, after a propagation over a length of $d/\cos\theta$, the radiative flux incident reaching the other end of the slab is $q_{inc}^{(2)} = \pi\tau I_t$ where

$$\tau = 2\int_0^{\pi/2} \exp^{-\kappa d/\cos\theta}\cos\theta\sin\theta d\theta \tag{B.1}$$

where κ is the slab's Planck-averaged absorption coefficient (Eq.(12)). A $\rho_{21}^d q_{inc}^{(2)}$ portion of this is reflected diffusely, and after another propagation over a $d/\cos\theta$ distance and transmission through the slab's interface upon which q_{inc} is incident, a quantity $q_R^{(2)} = \rho_{21}^d(1-\rho_{21}^d)(1-\rho_{12}^d)\tau^2 q_{inc}$ emerges back into medium 1 alongside $q_R^{(1)}$. Accounting for all the reflections, we get the equivalent diffuse reflectivity of the slab as

$$\begin{aligned} R_{slab}^d &= \rho_{12}^d + \rho_{21}^d(1-\rho_{12}^d)(1-\rho_{21}^d)\tau^2\sum_{i=0}^{i=\infty}(\rho_{21}^d\tau)^{2i} \\ &= \rho_{12}^d + \frac{\rho_{21}^d(1-\rho_{12}^d)(1-\rho_{21}^d)\tau^2}{1-(\rho_{21}^d\tau)^2} \end{aligned} \tag{B.2}$$

which is the well-known slab equation where the propagation factor $\exp^{-\kappa d/\cos\theta}$ has been replaced by τ under the assumption of diffuse reflection and transmission approximation. The slab's diffuse transmissivity T_{slab}^d is found in a similar way, and the diffuse absorptivity A_{slab}^d is obtained from the conservation of energy; $R_{slab}^d + T_{slab}^d + A_{slab}^d = 1$. Usually, the slab's emissivity ϵ is set equal to its absorptivity.

However in the present case, in order to be able to use the same formulae as for opaque materials - Eqs.(33,34,C.2), the additional energy flow through the cells caused by the medium's semi-transparency is modelled as an increased rate of emission whereby the transmissivity is incorporated into the equivalent diffuse emissivity of the slab which is then defined as

$$\begin{aligned} \epsilon_{slab}^d &= A_{slab}^d + T_{slab}^d = 1 - R_{slab}^d \\ &= \frac{(1-\rho_{12}^d)(1-\rho_{21}^d\tau^2)}{1-\rho_{21}^2\tau^2} \end{aligned} \tag{B.3}$$

which amounts to treating the transmitted part of an energy flux incident upon a slab as being emitted by the slab. Throughout section 4, Eq.(B.3) is used for semi-transparent materials in formulae derived for opaque materials.

Appendix C. Derivation of S_R^*=f(N_{rc}) and k_{eq}

Let $\Delta Q = Q_{N+1} - Q_N$. Ignoring the thermal coupling between conductive and radiative transports, we can break

down ΔQ into contributions from radiative and conductive transfers

$$\Delta Q_N = \Delta Q_N^c + \Delta Q_N^r \tag{C.1}$$

Looking at the radiative contribution first we can write (see, for example, Modest [41]):

$$Q_N^r = \sigma S_0 \frac{T_h^4 - T_c^4}{\sum_{i=1}^{i=N-1} \{1/\epsilon_i + 1/\epsilon_{i+1} - 1\}} \tag{C.2}$$

where $S_0 = (D_h - 2t)d$ is the surface of emission (d is the depth), and gaseous radiative flows to the lateral sides have been neglected. This equates to seeing the cells as a network of infinitely large radiative shields. This assumption is justified for wide and narrow cells, which holds for small enough values of S_R. But when S_R is small, *i.e* when N is large, we may write, to a good approximation:

$$\begin{aligned}\sum_{i=1}^{i=N} \{1/\epsilon_i + 1/\epsilon_{i+1} - 1\} &\simeq \sum_{i=1}^{i=N-1} \{1/\epsilon_i + 1/\epsilon_{i+1} - 1\} \\ &\simeq N(2 < \bar{\epsilon} > -1)\end{aligned} \tag{C.3}$$

where $< \bar{\epsilon} >$ is the inverse of the emissivity averaged between T_c and T_h. This yields

$$\begin{aligned}\Delta Q_N^r &= Q_{N+1}^r - Q_N^r \\ &\simeq \sigma S_0 (T_h^4 - T_c^4) \\ &\times \left(\frac{1}{(N+1)(2 < \bar{\epsilon} > -1)} - \frac{1}{N(2 < \bar{\epsilon} > -1)} \right) \\ &= -\frac{\sigma S_0}{N(N+1)} \frac{T_h^4 - T_c^4}{2 < \bar{\epsilon} > -1}\end{aligned} \tag{C.4}$$

This is the final expression for ΔQ_N^r and shows that to inhibit radiative transfers, as many cells as possible are necessary. However, the thermal gain decreases with increasing N with an inverse square law $\Delta Q_N^r \propto 1/N^2$.

The conductive contribution is treated in a similar way. Assuming a one-dimensional conductive flow with the lateral columns (conductive resistance $R_0 = D_h/(2td < k_s >)$) acting in parallel to the gas cells, themselves modelled as a series of gas and solid elements (conductive resistance R_N^g and R_N^s, respectively), the conductive resistance of the honeycomb may be expressed as

$$R_N = \frac{1}{1/R_0 + 1/(R_N^g + R_N^s)} \tag{C.5}$$

Using $R_N^s \ll R_N^g$ and $R_0 \ll R_N^g$, we may write

$$R_N \approx R_0(1 - R_0/R_N^g) \tag{C.6}$$

The variation of this conductive resistance is

$$\Delta R = R_{N+1} - R_N \approx R_0^2(1/R_N^g - 1/R_{N+1}^g) \tag{C.7}$$

which gives, with $R_N^g = N h_N / < k_g > S_0$:

$$\Delta R \approx -R_0^2 \frac{< k_g > S_0 t}{N(N+1)h_N h_{N+1}} \tag{C.8}$$

where h_N is the cell size when N cells are present and where it was assumed that the gaseous conductivity is so small that it is little dependent on h_N when h_N is small enough. As expected, ΔR is negative, which means that some conductive resistance is lost with the addition of an extra cell. Besides, the fact that it is proportional to $< k_g >$ in the $< k_g > \ll < k_s >$ limit can seem counter-intuitive, but is explained as follows. As the gaseous conductivity approaches zero, its resistance becomes infinitely large. At this point, any amount of gas will have an infinitely large resistance, so that adding an extra cell (*i.e* decreasing the volume of gas), will have very little effect on the total conductive resistance which will still be infinitely large. This is visible in Eq.(C.8) which leads to $\Delta R/R_0 \propto R_0 < k_g >$ which is infinitely small. The result is that the lower the gaseous conductivity, the smaller ΔR, which is what Eq.(C.8) shows.

We can now derive an expression for ΔQ_N^c:

$$\Delta Q_N^c = -(T_h - T_c)\frac{\Delta R}{R_N R_{N+1}} \approx -(T_h - T_c)\frac{\Delta R}{R_0^2} \tag{C.9}$$

which, together with Eq.(C.8), gives

$$\Delta Q_N^c = (T_h - T_c)\frac{< k_g > t S_0}{N(N+1)h_N h_{N+1}} \tag{C.10}$$

The final step is to find an expression for Q_N. Only accounting for conductive flows through the side column, we have, per unit depth

$$Q_N^c \simeq Q_1^c \simeq \frac{< k_s > (T_h - T_c) 2t}{D_h} \tag{C.11}$$

Besides, following from the above radiative developments, we have

$$\begin{aligned} Q_N^r &\simeq \sigma \frac{(T_h^4 - T_c^4) S_0}{N(2 < \bar{\epsilon} > -1)} \simeq \frac{Q_1^r}{N} \\ \Delta Q_N^r &\simeq -\frac{Q_1^r}{N(N+1)} \end{aligned} \tag{C.12}$$

It follows that

$$\frac{\Delta Q_N}{Q_N} = \frac{\Delta Q_c + \Delta Q_r}{Q_1^c + \frac{Q_1^r}{N}} = \frac{\frac{\Delta Q_c}{Q_1^c} - \frac{Q_1^r}{N(N+1)Q_1^c}}{1 + \frac{Q_1^r}{NQ_1^c}} \tag{C.13}$$

Recalling the definition of N_{rc} (Eq.(31)), and with Eqs.(C.10,C.11), we get

$$\frac{\Delta Q_N}{Q_N} \simeq \frac{\frac{<k_g> D_h (D_h - 2t)}{2 <k_s> h_n h_{N+1}} - N_{rc}}{N(N+1)(1 + \frac{N_{rc}}{N})} \tag{C.14}$$

which leads to Eq.(34).

Neglecting the conduction term, it can be shown that Eq.(34) becomes

$$N^2 + (1 + N_{rc})N + N_{rc}(1 - \frac{1}{\alpha}) > 0 \tag{C.15}$$

Finally, N^* is the root of this equation:

$$N^{*^2} + (1 + N_{rc})N^* + N_{rc}(1 - \frac{1}{\alpha}) = 0 \tag{C.16}$$

The positive root is given by Eq.(35). The approximation which consists in neglecting the conduction term in Eq.(34) can be shown to be justified for all values of D_h and N used here.

Next, for k_{eq}, we have, under the same assumptions:

$$k_{eq} = \frac{Q_N}{T_h - T_c} \approx \frac{Q_N^c + Q_N^{cell} + Q_N^r}{T_h - T_c} \tag{C.17}$$

where the global energy flow has been split into its radiative and conductive parts, and Q_N^{cell} is the conductive flow through the gas cells and solid walls. Therefore

$$\begin{aligned} Q_N^c &\simeq \frac{2t < k_s > (T_h - T_c) S_0}{D_h} \\ Q_N^r &\simeq \frac{Q_1^r}{N} \\ Q_N^{cell} &\simeq \frac{T_h - T_c}{R_N} \end{aligned} \tag{C.18}$$

where R_N is given by Eq.(C.6). When plugged into Eq.(C.18), together with $N h_N = D_h - (N+1)t$, this yields

$$k_{eq} \simeq \frac{2t < k_s >}{D_h} \left(1 + \frac{N_{rc}}{N}\right) + \frac{< k_g >}{1 - (N+1)t/D_h} \tag{C.19}$$

which is Eq.(40).